

Conductance Model for Extreme Events : Impact of Auroral Conductance on Space Weather Forecasts

Agnit Mukhopadhyay¹, Daniel T. Welling², Michael W. Liemohn¹, Aaron J. Ridley¹, Shibaji Chakraborty³, and Brian J. Anderson⁴

¹Climate and Space Sciences and Engineering Department, University of Michigan, Ann Arbor, MI, USA

²Department of Physics, University of Texas at Arlington, Arlington, TX, USA

³Department of Electrical and Computer Engineering, Virginia Polytechnic Institute and State University,

Blacksburg, VA, USA

⁴Applied Physics Laboratory, Johns Hopkins University, Baltimore, MD, USA

Key Points:

- An updated auroral conductance module is built for global models using non-linear regression & empirical adjustments spanning extreme events.
- Expanded dataset raises the ceiling of conductance values, impacting the polar cap potential, dB/dt & ΔB predictions during extreme events.
- Application of expanded model with empirical oval adjustments refines the conductance pattern, and drastically improves dB/dt predictions.

Corresponding author: Agnit Mukhopadhyay, agnitm@umich.edu

17 **Abstract**

18 Ionospheric conductance is a crucial factor in accurately estimating the closure of mag-
 19 netospheric currents in the ionosphere. Despite its importance in predictive investiga-
 20 tions of the magnetosphere - ionosphere coupling, the estimation of ionospheric con-
 21 ductance in the auroral region is precarious in most global first-principles based models. This
 22 imprecision in estimating this auroral conductance impedes both our understanding
 23 of the magnetosphere-ionosphere system during extreme space weather events, and pre-
 24 dictive capabilities of ground-based magnetic perturbations during extreme driving which
 25 generate geomagnetically induced currents. In this article, we address this concern, with
 26 the development of an advanced Conductance Model for Extreme Events (CMEE) that
 27 estimates the auroral conductance from field aligned current values. CMEE has been de-
 28 veloped using nonlinear regression over a year's worth of one-minute resolution output
 29 from assimilative maps, specifically including times of extreme driving of the solar wind-
 30 magnetosphere-ionosphere system. The model also includes provisions to enhance the
 31 conductance in the aurora using additional adjustments to refine the auroral oval. CMEE
 32 has been incorporated within the Ridley Ionosphere Model (RIM) of the Space Weather
 33 Modeling Framework (SWMF) for usage in space weather simulations. This paper com-
 34 pares performance of CMEE against the existing conductance model in RIM, through
 35 a validation process for six space weather events. The performance analysis indicates over-
 36 all improvement in the ionospheric feedback to the magnetosphere. Specifically, the model
 37 is able to improve the prediction of ionospheric currents which impact the simulated dB/dt
 38 and ΔB , resulting in substantial improvements in dB/dt predictive skill.

39 **Plain Language Summary**

40 Electric currents generated in the Earth's space environment due to its magnetic
 41 interaction with the Sun leads to charged particle deposition and closure of these cur-
 42 rents in the terrestrial upper atmosphere, especially in the high latitude auroral region.
 43 The enhancement in the electrical charge carrying capacity as a result of this process in
 44 the Earth's upper atmosphere, also known as the ionosphere, is challenging to estimate
 45 in most numerical simulations attempting to study the interactive dynamic and chem-
 46 ical processes in the near-Earth region. The inability to accurately estimate this quan-
 47 tity leads to underprediction of severe space weather events that can have adverse im-
 48 pacts on man-made technology like electrical power grids, railway and oil pipelines. In
 49 this study, we present a novel modeling approach to address this problem, and provide
 50 global simulations with a more accurate estimate on the electrical conductivity of the
 51 ionosphere. Through this investigation, we show that the accurate measurement of the
 52 charge carriers in the ionosphere using the new model causes substantial improvements
 53 in the prediction of space weather on the ground, and significantly advances our under-
 54 standing of global dynamics causing ground-based space weather.

55 **1 Introduction**

56 The interaction of the solar wind and the terrestrial magnetic field produces mag-
 57 netospheric current systems such as field aligned currents (FACs) which close through
 58 the conductive ionosphere, thereby allowing magnetospheric convection to eventuate (e.g.
 59 Axford & Hines, 1961; Dungey, 1963; Iijima & Potemra, 1976). For precise investigations
 60 of the magnetospheric feedback on the ionosphere and vice versa, an accurate estimate
 61 of the ionospheric conductance is critical for realistic global modeling of the magneto-
 62 sphere, especially during space weather events (e.g. Merkine et al., 2003, Ridley et al.,
 63 2004, Merkin, Sharma, et al., 2005; Merkin, Milikh, et al., 2005, Liemohn et al., 2005).
 64 Two dominant sources contribute to the ionosphere's enhanced but finite conductivity
 65 - solar extreme ultra-violet (EUV) flux on the dayside, and auroral precipitation in the
 66 polar region predominantly on the nightside (Schunk & Nagy, 2009; Newell et al., 2009;

67 Fuller-Rowell & Evans, 1987). Conductance due to solar EUV radiation is relatively well
 68 understood through the use of radiative transfer (e.g. Chapman, 1931). The EUV flux
 69 is accounted for in most modern modeling tools as a physics-based empirical function
 70 of the solar zenith angle (e.g., Brekke & Moen 1993). Auroral electron and ion precip-
 71 itation, largely driven by magnetospheric processes, further ionizes neutrals and ions in
 72 the ionosphere (e.g., Frahm et al., 1997; Ahn et al., 1998), and enhances the electrical
 73 conductivity in the high-latitude auroral regions (Robinson et al., 1987). Since auroral
 74 precipitation of charged particles is directly related to variations in the intrinsic mag-
 75 netic field (e.g., Roederer, 1970), auroral conductance is an important quantity to pre-
 76 dict when investigating the ionosphere's impact on the magnetosphere, and vice versa,
 77 during strong driving when the global magnetic field changes rapidly (e.g., Welling, 2019).

78 Although several studies have examined the influence of the ionospheric conduc-
 79 tance on the global state of the magnetosphere, ionospheric dynamics and their coupled
 80 non-linear feedback system (e.g., Raeder et al., 2001; Ridley et al., 2001, 2004; Liemohn
 81 et al., 2005; Wiltberger et al., 2001, 2004; Zhang et al., 2015; Connor et al., 2016; Oz-
 82 turk et al., 2017), few studies have actually explored the contribution of conductance on
 83 space weather forecasts, especially during extreme space weather events. This is very dif-
 84 ficult to do with data, since measurements of the ionospheric conductance are notori-
 85 ously inaccurate (Ohtani et al., 2014). Investigations using global models such as Rid-
 86 ley et al. (2004) have indulged in the broad quantification of the conductance due to EUV
 87 illumination and auroral precipitation. Studies such as Wiltberger et al. (2001), Zhang
 88 et al. (2015), Yu et al. (2016) and Wiltberger et al. (2017) addressed this further by iden-
 89 tifying the source and impact of various contributors to the auroral conductance. Ad-
 90 ditional evaluations by Perlongo et al. (2017) included the effect of auroral precipitation
 91 due to the ring current using a kinetic ring current model coupled to an ionosphere-thermosphere
 92 model. Modeling efforts by Ahn et al. (1998), Newell et al. (2009), Korth et al. (2014)
 93 have estimated ionospheric auroral conductance through empirical relations, using global
 94 quantities like solar wind input, ground-based magnetic perturbations and field aligned
 95 currents as inputs. Recently, Robinson et al. (2018) developed an empirical model us-
 96 ing incoherent scatter radar measurements against AMPERE FAC estimations, which
 97 spanned the St. Patrick's Day Storm of 2015, an event studied extensively for ionospheric
 98 disturbances (e.g., Le et al., 2016). In spite of its importance, the impact of auroral con-
 99 ductance during extreme events in global simulations has been hard to determine, due
 100 to inaccuracies in conductance estimations within global models, leading to possible un-
 101 derprediction of global quantities like cross polar cap potential (e.g., Honkonen et al.,
 102 2013; Mukhopadhyay, 2017), field aligned currents (Anderson et al., 2017), storm indices
 103 (Liemohn, McCollough, et al., 2018) and transient ground-based magnetic perturbations
 104 (Welling et al., 2018).

105 With rising operational usage of first-principles-based geospace models in space weather
 106 prediction, the need for accurate conductance models is even more necessary. Operational
 107 forecasts of the near-Earth space environment using first-principles based global numer-
 108 ical frameworks (e.g., Tóth et al., 2005), combining global magnetohydrodynamic (MHD)
 109 models (e.g., Powell et al., 1999; Raeder et al., 2001) with suitable inner magnetospheric
 110 models (e.g., De Zeeuw et al., 2004) and ionospheric models (e.g., Ridley & Liemohn,
 111 2002; Wiltberger et al., 2004), have been in use for space weather prediction (Liemohn,
 112 Ganushkina, et al., 2018) since the end of the GEM Challenge of 2008-09 (Pulkkinen et
 113 al., 2011, 2013, Rastaetter et al. 2013). The procedural assessment specifically presented
 114 in Pulkkinen et al. (2013) (hereinafter referred to as *Pulkkinen2013*) to investigate pre-
 115 dictive skill of global first-principles-based models in predicting ground-based magnetic
 116 perturbations dB/dt , initiated the transition of model usage toward operational predic-
 117 tion at the NOAA Space Weather Prediction Center (SWPC). Several investigations, since
 118 then, have further reviewed and systematically addressed the results from this effort, and
 119 have suggested rectifications to improve predictive skill (e.g., Honkonen et al., 2013; Glo-
 120 cker et al., 2016; Anderson et al., 2017; Mukhopadhyay, 2017; Liemohn, Ganushkina, et

121 al., 2018; Liemohn, McCollough, et al., 2018; Welling et al., 2018). In particular, the study
 122 by Welling et al. (2017) indicated inherent deficiencies in auroral conductance models
 123 used in global models that inhibited them from estimating conductance accurately dur-
 124 ing extreme space weather events. The study concluded that the inability of global mod-
 125 els to estimate the ionospheric conductance accurately during extreme events led to un-
 126 derprediction of dB/dt .

127 A key conclusion in the study by Welling et al. (2017) (hereinafter referred to as
 128 *Welling2017*) questions the dataset used in estimating a geospace model's auroral con-
 129 ductance during extreme weather, and hypothesizes that the inclusion of information from
 130 a larger dataset, including sufficient coverage of extreme events, may lead to improve-
 131 ments in a model's space weather predictive metrics during extreme events. The study
 132 falls short of addressing supplementary effects due to the auroral oval's pattern estima-
 133 tion in aforementioned models, and the acute effect such a pattern may have on predic-
 134 tive skill. In this paper, we describe the development and validation of an updated em-
 135 pirical auroral conductance model, specifically including data that spans several extreme
 136 events, which addresses the concerns raised in *Welling2017*. We use this conductance model
 137 within the geospace variant of the Space Weather Modeling Framework (SWMF; Tóth
 138 et al., 2005, 2012), identical to the version used operationally at the NOAA Space Weather
 139 Prediction Center for space weather forecasting, to investigate the effect of this enhanced
 140 conductance model on space weather predictions, and compare these results to the already-
 141 existing conductance model within the SWMF. We additionally study the effect of ad-
 142 justing the pattern of the auroral oval using empirical enhancements based on field aligned
 143 current strength, to alter the model's space weather predictions. As a result, in this ar-
 144 ticle, we investigate three major science questions:

- 145 1. Addressing *Welling2017*: Does expanding the dataset used to create the initial
 146 conductance model help improve space weather predictions?
- 147 2. How significant is the improvement in the space weather predictions due to the
 148 enhanced auroral oval adjustment parameters?
- 149 3. Can the combination of the expanded dataset and an auroral oval enhancement
 150 cause significant improvement in the global model's space weather prediction?

151 In order to address the aforementioned questions, a new **C**onductance **M**odel for **E**x-treme
 152 **E**vents (CMEE) has been developed. CMEE is based on the SWMF's empirical au-
 153 roral conductance model, which uses an inverse-exponential relation to estimate the con-
 154 ductance, and employs an empirically-driven auroral oval adjustment to enhance con-
 155 ductance in regions of strong FACs. A key difference in CMEE, however, is in the dataset
 156 it was developed from: CMEE uses one whole year of AMIE data to estimate its con-
 157 ductance. Compared to the old model which was derived from the relatively quiet month
 158 of January 1997, minute-data from the whole year of 2003 was utilized to develop CMEE.
 159 This included some of the most extreme geospace events ever observed (Cid et al., 2015).
 160 In addition to an enlarged training dataset, the value of the empirical coefficients in CMEE
 161 are deduced using a non-linear fitting algorithm with suitable extreme boundary con-
 162 ditions that minimizes the absolute error and maximizes the prediction efficiency. The
 163 global model configurations used and the science questions addressed in this study, and
 164 the subsequent results from this study are described in Sections 2 and 3 respectively, while
 165 the algorithm used to develop the advance conductance model and the auroral oval ad-
 166 justment module have been described in Section 2.2.

167 2 Methodology

168 2.1 Simulation Setup

169 The SWMF is a flexible framework that executes, synchronizes and couples many
 170 otherwise independent models together as one. It has performed favorably in predictive

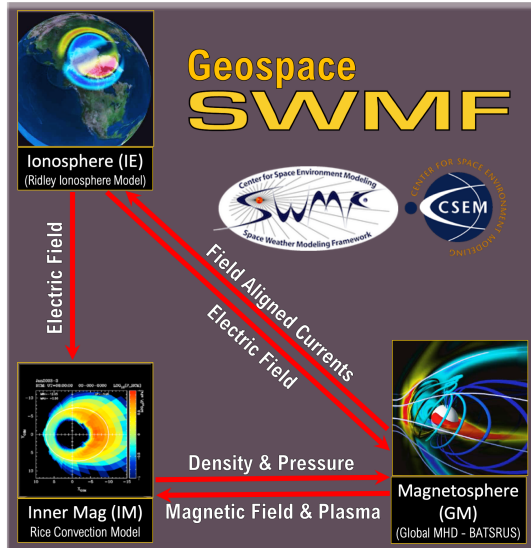


Figure 1. Component layout of the geospace version of the SWMF, same as the layout in *Pulkkinen2013*, used in this study to investigate the role of auroral conductance in space weather prediction.

metric challenges and investigations (e.g., *Pulkkinen2013*; Honkonen et al., 2013; Mukhopadhyay, 2017; Welling et al., 2017; Liemohn, McCollough, et al., 2018), contains an easily-modifiable empirical conductance model in the ionospheric electrodynamics module (Ridley et al., 2004), and is capable of calculating perturbations to the magnetic field (ΔB) by applying Biot-Savart integrals across its domain to estimate magnetometer values virtually (Yu et al., 2010). For this study, we have used the SWMF with three physical modules activated (Figure 1; details below). Identical to the study conducted by *Pulkkinen2013*, the SWMF's geospace version was configured to use three components: Global Magnetosphere (GM), Inner Magnetosphere (IM), and Ionospheric Electrodynamics (IE).

The GM module uses the Block Adaptive Tree Solar-Wind Roe Upwind Scheme (BATS-R-US, Powell et al., 1999; Gombosi et al., 2003) model which solves for the ideal non-relativistic magnetohydrodynamic (MHD) equations in the magnetosphere with an inner boundary at ~ 2.5 Earth radii (R_E). The computational domain for geospace simulations of BATS-R-US extends from $32R_E$ upstream to $224R_E$ downstream in the x direction and $128R_E$ in the y and z coordinates (GSM). The key feature of BATS-R-US is its flexible, block-adaptive Cartesian grid that reserves the highest resolution to regions of interest, ensuring the best combination of performance and accuracy.

The IM region is characterized by closed magnetic field lines and particles of keV energies. This module uses Rice Convection Model (RCM; Wolf et al., 1982). RCM solves for the bounce averaged and isotropic but energy resolved particle distribution of electrons and various ions. RCM receives flux tube volumes from BATS-R-US and returns the pressure and density values to correct those calculated within GM (De Zeeuw et al., 2004). It receives the ionospheric electric potential from the 2-dimensional IE module. The density and temperature initial and boundary values are computed from the GM solution.

The IE component calculates height integrated ionospheric quantities at an altitude of about 110 km. To do so, it receives field aligned currents (FACs) from GM and uses the Ridley Ionosphere Model (RIM, Ridley et al. 2001; Ridley & Liemohn 2002; Ri-

199 dley et al. 2004), a finite-difference Poisson solver, to calculate the electric potential and
 200 horizontal currents using a *prescribed* but dynamic conductance pattern. The module
 201 maps FACs at 3.5 Earth radii (R_E) over a two dimensional ionospheric domain, solves
 202 for the resulting potential using Ohm's Law (Goodman, 1995), and returns this value
 203 to GM and IM. The functioning of and developments to the ionospheric conductance model
 204 of RIM are the key features of this article, and are discussed in detail in Section 2.2, along
 205 with the development of a more advanced empirical conductance model, CMEE, as a re-
 206 placement to the aforementioned model.

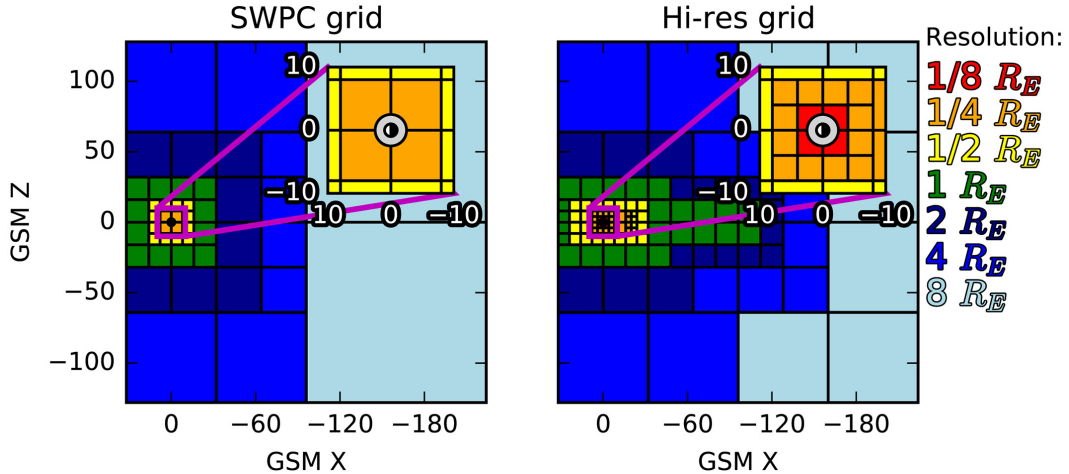


Figure 2. X-Z cuts showing cell sizes in the two MHD grids (reproduced from Haidupek et al., 2017). (Left) The grid used for the *SWPC* configuration (minimum cell size of $0.25 R_E$). (Right) The higher-resolution grid used for the *Hi-Res SWPC* configuration (minimum cell size of $0.125 R_E$)

207 In order to simulate a given event, we drive the model using solar wind velocity,
 208 magnetic field, density, and temperature, which are used to specify the upstream bound-
 209 ary condition of BATS-R-US. The only other input parameter is F10.7 flux, which is used
 210 by IE in computing the dayside EUV-driven ionospheric conductivity (Moen & Brekke,
 211 1993; Ridley et al., 2004). Simulation parameters have been kept similar to *Pulkkinen2013*,
 212 throughout the study; the model input conditions and parameters are not tailored to in-
 213 dividual events. For this study, we have simulated the events using two different reso-
 214 lutions of BATS-R-US : *SWPC* and *Hi-Res SWPC* (see Figure 2). The *SWPC* config-
 215 uration is nearly identical to the *Pulkkinen2013* study, and is used operationally by the
 216 Space Weather Prediction Center (SWPC). This grid (Figure 2, left) has cell sizes rang-
 217 ing from $8 R_E$ in the distant tail to $0.25 R_E$ at the inner boundary, a $16 R_E$ diameter
 218 cube surrounding the Earth, and contains around 1 million cells. The other configura-
 219 tion, *Hi-Res SWPC*, is similar to the previous configuration but uses a higher-resolution
 220 grid (among other modifications), to help resolve field aligned currents at the spatial in-
 221 ner boundary. The cell size of this grid (Figure 2, right) varies from $8 R_E$ in the tail to
 222 $0.125 R_E$ near the Earth, and contains ~ 1.9 million cells. For a detailed description of
 223 the above configurations, please refer to Welling & Ridley (2010) and Haidupek et al. (2017).

224 2.2 Estimation of Auroral Conductance in SWMF

225 For Ohm's Law to be solved within IE, knowledge of the ionospheric conductance
 226 tensor must be known *a priori* (e.g., Goodman, 1995). Within RIM, the legacy code es-
 227 timating the ionospheric conductance (Ridley et al., 2004) distinguishes two dominant

sources of ionospheric conductance: solar EUV conductance on the dayside, and the auroral precipitative conductance in the polar regions. Supplementary sources of conductance, like nightside "starlight" conductance, seasonal dependencies and polar rain, are added as either functions of the dominant sources of conductance, solar zenith angle or scalar constants. The solar EUV component to the conductance is dependent on the absorption and ion production function of the atmosphere as a function of the solar zenith angle, and is therefore straightforward to estimate using radiometry; the model described in Moen & Brekke (1993) is used to estimate this component of the conductance in most global models (e.g. Raeder et al., 2001 Wiltberger et al., 2004), including RIM. The conductance due to ion and electron precipitation in the auroral region is harder to predict, as this would require the precise knowledge of the charged particle distribution in the magnetosphere. While a physics-based approach to precipitation has been applied in several global models (e.g. Raeder et al., 2001, Zhang et al., 2015, Yu et al., 2016, Perlongo et al., 2017) using kinetic theory (e.g. Knight, 1973), RIM uses a different and simpler approach to estimate the auroral conductance.

2.2.1 Functioning of the Ridley Legacy Model

The auroral conductance module in RIM (briefly described in Ridley et al., 2004), hereinafter referred to as the Ridley Legacy Model (RLM), uses the magnitude and direction of FACs to empirically determine the auroral conductance. This is similar to existing statistical models constructed using FACs to predict and examine precipitation in the auroral ionosphere (e.g. Ahn et al., 1998, Korth et al., 2014, Carter et al., 2016, Robinson et al., 2018). While the numerical domain of RIM spans the entire ionosphere, the RLM domain is considerably limited, spanning from the magnetic pole to magnetic latitude of 60° for all magnetic local times (MLT). The auroral conductance at a given magnetic latitude and MLT is assumed to have the form:

$$\Sigma_{HorP} = A_0 - A_1 e^{-A_2^2 |J_{||}|} \quad (1)$$

where Σ_{HorP} denotes the auroral Hall or Pedersen Conductance in the ionosphere (in siemens), $J_{||}$ denotes the field aligned current density (in $\mu A/m^2$), and A_0 , A_1 (in siemens) and A_2 (in $m/\mu A^{-1/2}$) are fitting coefficients dependent on location Note that this inverse exponential relation is different from the one mentioned in Ridley et al. (2004); this was a typographical error and the actual relation is given by Equation 1.

The empirical coefficients are the result of fitting based off of conductance and field-aligned current maps derived from assimilative maps of ionospheric electrodynamics (AMIE; Richmond & Kamide, 1988; Kihl & Ridley, 2005) for the month of January 1997 (Boonsiriseth et al., 2001), using ground magnetic perturbations from ∼154 ground-based magnetometers. AMIE derives the auroral conductance using the formulation in Ahn et al. (1998) and Lu et al. (1997), which relate ground-based magnetic perturbations to the Hall and Pedersen conductance, and FACs. The month of runs encompasses ∼45,000 two-dimensional maps of Hall and Pedersen conductance and field-aligned currents. In addition to the empirical maps defining the conductance using FACs, additional auroral oval adjustments were applied to constrain and enhance the conductance in regions of strong FAC driving.

2.2.2 Conductance Adjustments in the Auroral Oval

The conductance pattern in RLM tends to produce broad regions of high conductance that are discontinuous between regions of strong FAC. To improve upon this, an adjustment to the conductance pattern is applied to the estimated pattern described above. The purpose of this is to create a channel for electrojets to form in the model and to improve on the overall electrodynamic result. Though this feature has been implemented in RLM for over a decade, this work is the first to formally describe it and evaluate its impact.

The algorithm for this adjustment starts by estimating the location of the auroral oval. Across all local time values (ϕ) in the model's grid, the geomagnetic co-latitude of the maximum upward FAC at that local time slice ($J_{max}(\phi)$) is obtained. The result is $\theta(\phi)$, or co-latitude as a function of local time. The mean co-latitude, θ_{mean} , weighted by $J_{max}(\phi)$, is then obtained as follows:

$$\theta_{mean} = \frac{\sum \theta(\phi) J_{max}(\phi)}{\sum J_{max}(\phi)} \quad (2)$$

A day-night shift in the center of the oval is calculated using the co-latitudes of $J_{max}(\phi)$ at noon and midnight:

$$\Delta\theta = \frac{J_{noon} * (\theta_{noon} - \theta_{mean}) - J_{midnight} * (\theta_{midnight} - \theta_{mean})}{J_{noon} + J_{midnight}} \quad (3)$$

Using these values, the location of the auroral oval is modeled as follows:

$$\theta(\phi)_{aurora} = \theta_{mean} + \Delta\theta \cos(\phi) \quad (4)$$

With the oval location set, an adjustment is applied to the conductance values about the oval by adjusting the fitting coefficients, A_0 and A_1 :

$$A_{0,adj} = A_0 e^{-\frac{d^2}{W^2}} \quad (5)$$

$$A_{1,adj} = A_0 - (A_0 - A_1) e^{-\frac{d^2}{W^2}} \quad (6)$$

...where, for each line of constant local time, d is the co-latitude distance from the oval's locus and W is the width of the oval (default is 2.5°). A baseline conductance about the oval is also applied to avoid nonphysical solutions in regions of low FACs:

$$\Sigma_{baseline} = 1.7(\Sigma_{HorP} + k e^{-\frac{d^2}{W^2}}) \quad (7)$$

where 1.7 is a factor meant to amplify the value of the conductance and k is a constant derived from the aggregate value of the AMIE-derived auroral conductance in regions of high precipitation (magnetic latitude $\in [65^\circ, 80^\circ]$). In this study, the value of k was found to be 7.5 siemens for Hall conductance, and 5 siemens for Pedersen conductance from the AMIE dataset. The net result of this adjustment is that, about the oval, the range of possible conductance values is narrowed and enhanced, and a coherent, sharper auroral conductance pattern arises.

2.2.3 Conductance Model for Extreme Events (CMEE)

Based on the same formulation as RLM, CMEE was developed using a larger dataset in order to include information during intense space weather events ($Dst < -150nT$). For this model, minute-resolution data from AMIE for the whole year of 2003 were utilized to estimate the new fitting coefficients. This significantly increased the model's base dataset from $\sim 45,000$ 2D maps used in RLM, to over $\sim 530,000$ 2D maps used in the present study. In addition to this, the value of the empirical coefficients in CMEE are deduced assuming the same empirical relationship between upward or downward FACs with Hall and Pedersen Conductance, as given by Equation 1. However, unlike RLM which estimates the fitting using equal weighting, the new fitting has been designed using a novel nonlinear regression algorithm which imposes sufficient boundary conditions to ensure that the fitted curve extends to these extreme values and is not just limited to the aggregate value of conductance. This was done by basing the max endpoints of the fittings on the 90% percentile of the FAC values.

Figure 3 (a) presents a representative line plot of Equation 1, and demarcates the conductance vs FAC space into bounded regions designed to estimate fitting coefficients.

The regression algorithm of CMEE classifies FAC data into low and high magnitude bins, separately for upward and downward FACs. The bin boundary for low magnitude FACs, including zero FACs was based on the approximate order of low magnitude FAC density, where asymptotic behavior of conductance values is prevalent and a median value could be found. The median value of the conductance populations in this FAC bin is the minima of the curve ($A_0 - A_1$). For the low FAC case, setting the bin boundary at $\pm 10^{-4} \mu\text{A}/\text{m}^2$ for both upward and downward field aligned currents at all locations led to optimum results. To deduce the conductance maxima as a constant asymptotic value, the FAC dataset was binned into 10 discrete bins with respect to the absolute value of FAC, and the median value of conductance in the bin with the highest FAC values (10th bin) was defined as A_0 . A Levenburg-Marquadt (e.g. Pujol, 2007) type bounded least-squares method was used to estimate the non-linear fitting coefficient A_2 . The fitting error was defined as the arithmetic mean of the median absolute percentage error (MAPE) and the median symmetric efficiency (ξ) ratio of the data, as defined in Morley et al. (2018). In order to avoid nonphysical solutions from the ionospheric solver due to large gradients (spikiness) in the conductance values, a smoothing filter was applied on the coefficients. The filter was based on a Laplacian mesh smoothing algorithm (e.g. Herrmann, 1976), commonly used in image processing (Yagou et al., 2002) and mesh refinement (Sorkine et al., 2004). The filter is applied such that at each node i ,

$$x_i = \begin{cases} x_i & \text{if } \frac{x_i - X}{X} \leq \lambda \\ X & \text{if } \frac{x_i - X}{X} > \lambda \end{cases} \quad (8)$$

where

$$X = \frac{1}{N} \sum_{j=1}^N x_j \quad (9)$$

Here, λ is the prescribed difference, N is the number of adjacent vertices to node i , x_j is the position of the j -th adjacent vertex and x_i is the new position for node i . The prescribed difference, similarly defined as the relative difference, is kept at 10%.

Figures 3(b) shows an example of the fitting using the regression algorithm mentioned above over a map of Hall conductance and FAC distribution from AMIE, at the geomagnetic latitude of 62° and MLT 23 for upward FACs. Figure 3(c) compares the fitting function using CMEE's regression with coefficients from RLM for the same geomagnetic location, but for both upward and downward FACs. The usage of a regression algorithm over a larger span of data shows visible differences in Figure 3(c), where CMEE, denoted in red, is able to push the max value of the conductance to better estimate the quantity during extreme driving. In addition, because of the usage of low FAC bins, the model is also able to provide uniformity in conductance values when field aligned currents are low and/or switch directions. This was previously not included in RLM, denoted in blue in Figure 3(c), as the coefficient values were estimated using uniform weighting on a case-by-case basis separately for upward and downward FACs.

2.3 Event Selection & Prediction Assessment

In order to evaluate CMEE's predictive capabilities and address the science questions mentioned in Section 1, we have simulated a range of space weather events listed in Table 1(a) using variations of the auroral conductance model within the SWMF for comparisons against observations. Since it is a de-facto standard in the space weather community, the present investigation chose to simulate the same events listed in Table 1 of the *Pulkkinen2013* study. Simulation of these events was administered for the two resolutions described in Section 2.1, and using four different variations of the conductance model :-

- 358 1. Using only the empirical coefficients of RLM to specify the aurora,
- 359 2. Using only the empirical coefficients of CMEE to specify the aurora,

- 360 3. Adjusting RLM estimates with the additional enhancements in the auroral oval,
 361 and
 362 4. Adjusting CMEE estimates with the additional enhancements in the auroral oval.

363 Table 1(b) lists the 8 sets of simulations resulting from the above combination.

364 The study uses data from satellite in-situ measurements and ground-based obser-
 365 vations for comparisons against model results. Cross polar cap potential (CPCP) from
 366 the model variants was compared against values obtained via the AMIE model and obser-
 367 vations from the Super Dual Auroral Radar Network (SuperDARN; e.g. Khachikjan
 368 et al., 2008). Since AMIE has a tendency to overpredict CPCP (e.g. Gao, 2012), obser-
 369 vations from the SuperDARN were also used to provide a range to the CPCP estimates.
 370 Integrated field aligned currents derived from observations by the Active Magnetosphere
 371 and Planetary Electrodynamics Response Experiment (AMPERE) mission (Anderson
 372 et al., 2014; Waters et al., 2020), estimated using the methodology in Anderson et al.
 373 (2017), were used to compare modeled values of FACs. In addition, magnetometer ob-
 374 servations from the 12 magnetometer stations listed in Table 2 of the *Pulkkinen2013* study
 375 were used to evaluate the predicted ground-based magnetic perturbation ΔB and its tem-
 376 poral variant dB/dt .

377 Using a similar approach as *Pulkkinen2013*, a binary event analysis (e.g. Jolliffe
 378 & Stephenson, 2012; Wilks, 2011) was used to construct a set of relevant performance
 379 metrics. An event is defined as the absolute value of a parameter-in-question (any phys-
 380 ical quantity like dB/dt) exceeding a predetermined event threshold at any time within
 381 a comparison window t_f . For each such window, four outcomes are possible: "Hit" or
 382 True Positive (TP; event is observed, and also predicted), "False Alarm" or False Pos-
 383 itive (FP; event is not observed, but predicted by model), "Miss" or False Negative (FN;
 384 event is observed, but not predicted), and "Correct No Events" or True Negative (TN;
 385 event is not observed, and not predicted). Similar to *Pulkkinen2013*, the analysis fore-
 386 cast window t_f was selected to be 20 minutes. The combined results from all events listed
 387 in Table 1(a) for a given simulation set are divided into discrete events by the forecast
 388 window, creating a contingency table accounting for TPs, FPs, FNs and TNs for a spe-
 389 cific threshold. Unlike the *Pulkkinen2013* study, this study chose to discretize the dB/dt
 390 into thresholds ranging from 0.1 nT/s to 1.7 nT/s at intervals of 0.1 nT/s, including the
 391 thresholds 0.3 nT/s, 0.7 nT/s, 1.1 nT/s and 1.5 nT/s which were used in the former study.
 392 In addition to dB/dt , the ΔB values have been discretized using thresholds obtained from
 393 Tóth et al. (2014) and *Welling2017*, ranging from 75 to 400 nT at intervals of 25 nT were
 394 used.

395 Once the contingency tables were prepared for each simulation variation, a com-
 396 bination of performance metrics were applied to study improvements. The metrics used
 397 in this study and their respective definitions are listed in Table 2. Amongst these met-
 398 rics, the top four are accuracy measures that help describe the improvement of individ-
 399 ual outcomes in a contingency table, while the bottom four metrics quantify the accu-
 400 racy of a prediction. The Probability of Detection (POD), also called the Positive Pre-
 401 diction Value, is the ratio of positive and negative results, and ranges from 0 to 1, with
 402 1 being a perfect score. The Probability of False Detection (POFD) is the ratio of misses
 403 against total negative results. POFD ranges from 0 to 1, with 0 being a perfect score.
 404 Along with the POD, these two ratios are accuracy measures of model discrimination.
 405 The False Alarm Ratio (FAR), also called False Positive Rate is the ratio between the
 406 number of negative events wrongly categorized as positive and the total number of ac-
 407 tual negative events (false negatives + true negatives). The Miss Ratio (MR) is defined
 408 as the ratio between the number of misses and the sum of hits & misses, describing the
 409 conditional probability of a negative test result given that the condition being looked for
 410 is present. Both FAR and MR range from 0 to 1, with 0 being a perfect score. These two
 411 metrics are a measure of model reliability. The Threat Score (TS), also known as Crit-

(a) List of Events

Event #	Date and Time
1	29 October 2003 06:00 UT - 30 October 06:00 UT
2	14 December 2006 12:00 UT - 16 December 00:00 UT
3	31 August 2001 00:00 UT - 1 September 00:00 UT
4	31 August 2005 10:00 UT - 1 September 12:00 UT
5	5 April 2010 00:00 UT - 6 April 00:00 UT
6	5 August 2011 09:00 UT - 6 August 09:00 UT

(b) List of SWMF Simulations

	<i>RLM Coeffs</i>	<i>CMEE Coeffs</i>	<i>RLM w OA</i>	<i>CMEE w OA</i>
<i>SWPC</i>	Set A	Set B	Set C	Set D
<i>Hi-Res SWPC</i>	Set E	Set F	Set G	Set H

RLM Coeffs - Empirical Coefficients of the Ridley Legacy Model

CMEE Coeffs - Empirical Coefficients of the Conductance Model for Extreme Events

RLM w OA - Ridley Legacy Model, with Auroral Oval Adjustments

CMEE w OA - Conductance Model for Extreme Events, with Auroral Oval Adjustments

Table 1. (a) List of space weather events used in this study to test and validate the different conductance models. This is the same set of events used in *Pulkkinen2013*. (b) A tabular description of all the simulations conducted for this study, binned by SWMF domain variations used: Each set of runs (denoted as 'SET \times ', where \times is the alphabetic value designated) is a simulation of all space weather events listed in (a), using a particular variation of the auroral conductance model (columns) within a given configuration of the SWMF (rows).

ical Success Index is the ratio of all true positives against the sum of total number of occurrences and false alarms. Due to its neglect of non-occurrences, this score is well suited for scoring predictions of rare events like extreme driving during space weather events. The F_1 score, another measure of a test's accuracy, is defined as the harmonic mean of the POD and the hit rate, given by $(1-MR)$. Similar to the Threat Score, the F_1 score reaches its best value at 1 and worst at 0. The True Skill Score (TSS) or Hanssen-Kuiper Skill Score (Hanssen & Kuipers, 1965) is a performance metric with values ranging from -1 to +1, with 0 representing no skill. The TSS is defined as the difference between the hit rate (given by $1 - MR$) and false alarm rate. Lastly, the Heidke Skill Score (HSS; Heidke, 1926) is a performance metric that measures the improvements in a model's results against random chance. Similarly to the TSS, the value of HSS ranges from -1 to +1, with 0 representing no skill. The HSS is popular in space weather forecasting, and has been established as a suitable comparative metric in several space weather studies (Welling & Ridley, 2010, *Pulkkinen2013*, T6th et al., 2014, Welling et al., 2018).

3 Results & Discussion

3.1 Impact on Global Quantities

Figure 4 exhibits the variations in the pattern and magnitude of Hall conductance for simulations using the low-res *SWPC* configuration. Each dial-plot column displays the high latitude Hall conductance at different time instances from the simulation sets A, B, C and D respectively. The first row shows results from 04:33 UT on October 29, 2003 : toward the beginning of Event 1, before the sudden commencement with the storm

Performance Metric	Acronym	Mathematical Definition
Probability of Detection	POD	$\frac{TP}{(TP+FP)}$
Probability of False Detection	POFD	$\frac{FN}{(FN+TN)}$
False Alarm Ratio	FAR	$\frac{FP}{(FP+TN)}$
Miss Ratio	MR	$\frac{FN}{(TP+FN)}$
Threat Score	TS	$\frac{TP}{(TP+FN+FP)}$
F_1 Score	F_1	$\frac{2TP}{(2TP+FP+FN)}$
True Skill Score	TSS	$\frac{TP}{TP+FN} - \frac{FP}{FP+TN} = (1 - MR) - FAR$
Heidke Skill Score	HSS	$\frac{2(TP \times TN - FP \times FN)}{((TP+FP)(FP+TN)+(TP+FN)(FN+TN))}$

Table 2. List of performance metrics used in this study.

433 index K_p less than 4. The second and third rows, titled Epoch 2 and Epoch 3, compare
 434 the four sets at 06:20 UT and 06:46 UT on the same day during the sudden commencement
 435 and main phase of Event 1, when $4 \leq K_p < 8$ and $K_p \geq 8$ respectively. As a
 436 reference, the bottom line plot shows the K_p throughout the event, along with the pre-
 437 dicted K_p from the four simulation variants with the background coloured by the mag-
 438 nitude of K_p - green for $K_p < 4$, yellow for $4 \leq K_p < 8$, and red for $K_p \geq 8$.

439 Comparing results of Sets A and B, the increased dataset used in CMEE increases
 440 the max value of conductance and is capable of capturing auroral dynamics across dif-
 441 ferent activity for every epoch. The addition of oval adjustments visibly alters the pat-
 442 tern of conductance - comparison of Sets A and B with their respective counterparts in
 443 Sets C & D illustrate how the adjustments intensify the conductance in regions of high
 444 field aligned currents, mimicking discrete arcs. The difference in Sets C & D, while not
 445 so apparent in Epochs 1 and 2, are substantially distinct in Epoch 3, when $K_p \geq 8$.
 446 In this case, the difference in the conductance caused by the combined usage of the in-
 447 creased dataset spanning extreme events and the additional oval-region enhancement re-
 448 sults in a higher conductance peak in Set D. For higher K_p , CMEE increases nightside
 449 conductance and lowers dayside conductance. This is because CMEE coefficients, a byprod-
 450 uct of an increased dataset spanning seasonal changes in addition to being estimated us-
 451 ing a nonlinear regression algorithm, computes lower dayside conductance and higher
 452 nightside conductance in comparison to the RLM coefficients. An unusual feature of us-
 453 ing FAC-directed empirical models is the emergence of islands of conductance during the
 454 peak of the storm (Epoch 3). These discontinuities are reduced by the initial usage of the
 455 smoothing function on the coefficients, and addition of a baseline value in the auroral
 456 oval region.

457 Figure 5 compares integrated field aligned currents (iFACs) observations during Event
 458 5 by AMPERE, against estimates from SWMF. Events 5 and 6 were observed by AM-
 459 PERE, and compared to models in Anderson et al. (2017). The iFACs were estimated
 460 similarly to Anderson et al. (2017) and were used to compare the effect of dataset ex-
 461 pansion in the top panel (a), the impact of oval adjustments in the middle panel (b), and
 462 the combined influence both in the bottom panel (c). In each of these panels, we com-
 463 pare the low resolution *SWPC* configuration of the SWMF simulations (Sets A, B, C
 464 and D) with the *Hi-Res SWPC* configuration simulations (Sets E, F, G and H) to vi-
 465 sualize the impact of conductance on the input conditions to IE. While minor variations
 466 are caused by the usage of different conductance models, no significant changes are ob-
 467 served either by using the CMEE coefficients or by adjusting the auroral oval. Instead,
 468 the results show the *Hi-Res SWPC* simulations being able to better capture the mag-
 469 nitude and dynamics of the iFACs than the *SWPC* configurations. While there are def-
 470 initive changes in the FACs and iFAC values due to the different auroral models, the in-

471 increased resolution helps to capture more of the FACs, dramatically improving the data-
 472 model comparison.

473 Figure 6 compares simulated cross polar cap potential (CPCP) for all simulation
 474 sets against values obtained from AMIE and SuperDARN, for Event 3, which was the
 475 only event in this study for which high quality AMIE and SuperDARN data were avail-
 476 able. Figure 6 is divided into three groups: in each group, the low res and high res sim-
 477 ulations are compared in separate subplots with the topmost group in part (a) illustrat-
 478 ing the impact of updated conductance coefficients on CPCP, middle group in part (b)
 479 investigating the impact of oval adjustments, and the bottom group in part (c) compar-
 480 ing the combined influence of dataset expansion and oval adjustments. The difference be-
 481 tween the AMIE CPCP, denoted by the solid black line, and SuperDARN CPCP, de-
 482 noted by the dot-dashed line, has been demarcated using a thick dark grey region in each
 483 subplot to give an envelope of expected values based on the observations-based estimates.

484 As shown in Figures 4 and 5, the introduction of CMEE and oval adjustments in-
 485 creases the value of the auroral conductance but does not dramatically impact the strength
 486 of FACs, for a given domain resolution. Since the electrostatic potential is the direct out-
 487 put of Ohm's Law, an increment in conductance with no substantial change in FACs leads
 488 to a lower value of CPCP. This is explicitly observed in part (a), where RLM-driven sim-
 489 ulations overestimates the CPCP in both the *SWPC* and *Hi-Res SWPC* cases, in com-
 490 parison to CMEE-driven simulations. The *Hi-Res* RLM case, denoted in yellow (Frame
 491 6a-ii), particularly stands out because the FAC-driven conductance reaches the ceiling
 492 set by the coefficient A_0 , i.e. as the magnitude of FACs increases, the value of conduc-
 493 tance attains the asymptotic maximum value (A_0) in the given model. Since the median
 494 A_0 value is higher in CMEE it is able to give a reasonable CPCP estimate, while RLM's
 495 reduced conductance peaks during the strongest driving resulting in the CPCP being an
 496 order of magnitude greater. In part (b), conductance increments driven by oval adjust-
 497 ments largely reduces the CPCP, except during the main phase of the event when $K_p >$
 498 4. This is because, during peak driving, the conductance from both models is so large
 499 that the oval adjustments do not affect results substantially. In part (c), CMEE-driven
 500 CPCP is lower than RLM-driven CPCP, as is expected. The CPCP values from Set D
 501 (Frame 6c-i) are too low, indicating that the model is overestimating the conductance
 502 which resulted in a lower CPCP. For the *Hi-Res* case in Frame 6c-ii, the higher conduc-
 503 tance estimation coupled with better resolved FACs acts in favour of CMEE-driven sim-
 504 ulations in Set H, and leads to a more realistic CPCP as shown by the comparison against
 505 AMIE and SuperDARN. In all events, simulations driven with RLM tend to have a higher
 506 CPCP compared to CMEE, as the conductance ceiling is higher in CMEE than RLM.

507 Figure 7 illustrates the impact of conductance on dB/dt predictions during Event
 508 2, at two magnetometer stations - the high-latitude magnetometer station at Yellowknife
 509 (YKC) located at magnetic latitude (MLat) 68.93° N and magnetic longitude (MLon)
 510 299.36° , and the mid-latitude magnetometer station at Newport (NEW) located at MLat
 511 54.85° N and MLon 304.68° . While YKC and NEW are far apart latitudinally, longi-
 512 tudinally they are separated by less than 5° , making them a good candidate to study
 513 the expansion of the auroral oval under strong driving conditions. The background in
 514 each subplot, in addition to being coloured by K_p similar to Figures 5 and 6, are dark-
 515 ened to indicate times when the magnetometer was on the nightside. Additionally, dash-
 516 dot lines in all subplots indicate the four thresholds chosen in the *Pulkkinen2013* study.

517 Between 14:08 UT and 18:17 UT on December 14, 2006, as activity increases, mas-
 518 sive dB/dt spikes were observed at YKC with values crossing the four *Pulkkinen2013* thresh-
 519 olds. These spikes died down as activity increased, indicated by the increment in the K_p
 520 values. From \sim 18:20 UT to 07:04 UT on December 15, except for one massive spike at
 521 04:28 UT, dB/dt spikes at YKC barely cross the second and third threshold. During this
 522 time period, the magnetometer was mostly on the nightside. Interestingly, all substan-
 523 tial perturbations observed at NEW occur during this same time interval, between 22:21

524 UT and 07:54 UT. This is an indication that the auroral oval expanded equatorward during
 525 this given time interval, with the storm intensifying. This expansion of the oval re-
 526 sulted in latitudinally-high YKC no longer being in the auroral zone and instead being
 527 in the polar cap region, while the lower boundaries of the auroral oval reached latitudinally-
 528 lower NEW. Starting at 07:54 UT, spikes at NEW died down and were almost negligi-
 529 ble throughout the rest of the event. Around the same time, massive spikes crossing all
 530 four thresholds were observed again at YKC as the magnetometer station approaches
 531 the midnight-dawn sector. The spikes at YKC were observed until 16:33 UT as the mag-
 532 netometer station rotated to the dawn-noon sector, through the recovery period of the
 533 event.

534 In parts (b) and (c) of Figure 7, modeled dB/dt at YKC and NEW are compared
 535 against observations. The topmost panel in part (b) compares modeled dB/dt from Sets
 536 E and F addressing the impact of dataset expansion. The middle panel in (b) compares
 537 Sets F and H to address the effect of auroral oval adjustments, while the bottom panel
 538 compares Sets G and H to study the combined influence of both the expanded dataset
 539 and the oval adjustments. In part (c), modeled dB/dt from Sets G and H are compared
 540 against observations at NEW. To simplify visualization, the minute-resolution data from
 541 both observed and modeled dB/dt values in parts (b) and (c) have been max-filtered for
 542 every 10 minute interval. Additionally, the subplot background and threshold lines in
 543 parts (b) and (c) are plotted and coloured similarly to part (a).

544 In the top panel of part (b), the magnitude of the CMEE-simulated dB/dt spikes
 545 are mostly at par with or moderately larger than the RLM-simulated spikes through most
 546 of the event. Both Sets E and F reasonably modeled the dB/dt during the time inter-
 547 val when the oval expanded and YKC was in the polar cap. However, they were unable
 548 to reproduce the heavy spikes that appeared both before and after the time interval, barely
 549 crossing the fourth threshold of 1.5 nT/s at any given instance. In the middle panel, both
 550 the frequency and magnitude of the dB/dt spikes increased significantly with the intro-
 551 duction of the oval adjustments. While this led to minor improvements in reproducing
 552 observations at time intervals when YKC observed heavy spikes, a substantial change
 553 occurred during the oval expansion when there were minimal dB/dt perturbations in both
 554 the observations and the coefficient-driven simulation results but intense spikes at high
 555 frequencies in the oval-adjusted simulation output. This increment in dB/dt spikes is dom-
 556 inant in the bottom panel of part (b) in both CMEE and RLM driven simulations. The
 557 impact of the dataset expansion combined with the oval adjustment in Set H simulations
 558 led to a sharp increase in the magnitude of the spikes, in addition to the sharp rise in
 559 frequency. Part (c) indicate that the model does not reproduce the dB/dt spikes at NEW,
 560 regardless of the conductance model used. This is in direct contrast to the results from
 561 the last panel of part (b) which compares the same model variants but shows multiple
 562 intense dB/dt spikes at YKC during the same time interval. This indicates that while
 563 usage of CMEE + oval adjustments improved the performance, there were still outstand-
 564 ing issues concerning the expansion and location of the oval that may require a more com-
 565 prehensive, physics-based approach.

566 Figure 8 illustrates comparison magnetic perturbations ΔB at the same magne-
 567 tometer stations during the same event to provide further clarity on the issue of auro-
 568 ral expansion. Part (a) compares the modeled and simulated ΔB at YKC and NEW dur-
 569 ing the event. At YKC, heavy fluctuations were observed in the ΔB values correspond-
 570 ing with the same time intervals when the massive spikes in dB/dt were observed in Fig-
 571 ure 7(a): between 14:21 UT and 18:19 UT, on December 14, and 06:42 UT and 17:07
 572 UT on December 15. The magnitude of ΔB were $\geq 500 \text{ nT}$ during these time intervals.
 573 At NEW, while all variations in ΔB were comparatively lower ($\leq 400 \text{ nT}$), heavy fluc-
 574 tuations were seen during the same time interval when the auroral oval expands and sig-
 575 nificant dB/dt perturbations in Figure 7(a) occur, between 23:37 UT and 12:07 UT. Dur-
 576 ing the oval expansion phase, YKC-observed ΔB increases steadily with time produc-

577 ing minimal fluctuations during this period, retroactively indicating why the dB/dt is
 578 low.

579 In parts (b) and (c) of Figure 8, the simulated ΔB from Sets G and H reasonably
 580 reproduce the observed ΔB pattern. During the oval expansion phase of the event, the
 581 simulated ΔB of both sets fluctuate with higher frequency and magnitude than is ob-
 582 served at YKC, thereby explaining the massive spikes in the simulated dB/dt seen dur-
 583 ing the same time interval in Figure 7(b). Quantitatively, the Set H simulations exhibit
 584 the best performance with a symmetric signed bias percentage (SSPB; Morley et al., 2018)
 585 of $\sim 5.6\%$. Here, SSPB measures the symmetric bias in the forecast against the observed
 586 values. At NEW, comparison of the simulated ΔB from either sets do not differ substan-
 587 tially with each other, with a negligible difference of $\leq 1\%$ in their respective SSPB. Nei-
 588 ther models are able to predict the perturbations during the main phase of the storm
 589 between 00:00 UT to 09:00 UT, explaining similarly poor performance in predicting the
 590 dB/dt values for this magnetometer. Part (d) compares the individual contributions of
 591 the global current systems - auroral Hall and Pedersen currents, field-aligned currents
 592 and magnetospheric currents, in the ΔB estimation at YKC and NEW from the Set H
 593 simulation. At YKC, auroral and field-aligned currents are the dominant current sys-
 594 tems driving perturbations in the magnetic field while magnetospheric currents contribute
 595 negligibly. The opposite is true at NEW, where the ΔB variations are mostly driven by
 596 changes in the magnetospheric currents and field aligned currents, with auroral currents
 597 barely affecting the simulated ΔB even during the peak driving of the system, indicat-
 598 ing minimal contribution.

599 The comparisons in Figures 7 and 8 indicate that in the modeled ΔB and dB/dt
 600 values, the auroral currents have little or no impact on mid and low latitude magnetome-
 601 ter predictions as the auroral oval is not able to extend equatorward to these latitudes.
 602 While this is expected during quiet conditions, the impact of auroral currents during ex-
 603 treme events can change dynamically with the expansion of the auroral oval, and can
 604 extend to much lower latitudes as evidenced by NEW during this event. The impact of
 605 this shortcoming on predictive skill has been described in further detail in Section 4.

606 3.2 Performance Quantification of dB/dt Comparisons

607 The results from the binary event analysis performed on the dB/dt predictions show
 608 that changing the auroral conductance in the global model, either by expanding the dataset
 609 or by applying the oval adjustments, led to minimal or no improvement in skill score for
 610 the lowest dB/dt threshold, but improved skill for the remaining dB/dt thresholds, with
 611 the most improvement in the highest thresholds. Table 3 presents a re-analysis of the
 612 results from Pulkkinen2013, emphasizing the changes in the HSS of dB/dt results, that
 613 were caused by CMEE and the auroral oval adjustments. In part (a) of the table, the
 614 expansion of dataset results in the improvement of HSS in each threshold for both the
 615 low and high resolution cases, as evidenced by the difference column. This addresses Welling2017's
 616 original question, that expansion of the dataset can lead to improvement in dB/dt pre-
 617 dictions. In part (b), the HSS improvement caused by oval adjustments to the aurora
 618 is more substantial than in part (a), with HSS going up by ~ 0.1 in the highest thresh-
 619 olds for both *SWPC* and *Hi-Res SWPC* configurations. The comparison of both RLM
 620 and CMEE combined with oval adjustments in case (c) show similar improvements in
 621 predictive skill for the higher dB/dt thresholds when using CMEE with oval adjustments.

622 Figures 9(a) and (b) provide a quantitative picture of HSS improvement in the dB/dt
 623 predictions over many more thresholds. In both subplots, the y -axis is HSS, while the
 624 increasing dB/dt thresholds on the x -axis provide a quantitative value of space weather
 625 activity. As expected, the HSS scores for all models decreased with increasing thresh-
 626 old value. However, in the most-extreme thresholds CMEE-driven simulations out-perform
 627 RLM-driven simulations, with improvements in the HSS of the same order as previously

evidenced in Table 3. The HSS values in the highest dB/dt thresholds for the low-resolution runs of CMEE, in both parts (a) and (b), were either at par or larger than the HSS values for not only the low-resolution but also the high-resolution RLM simulations. This is a significant improvement in the skill score due to CMEE, as this provides an alternate physics-based remedy that otherwise could only be solved numerically. Naturally, the HSS values of the high-resolution CMEE-driven simulations were the highest at almost all thresholds. Using this result, we can partially address the science questions posed in Section 1 that the auroral conductance impacts the dB/dt significantly, and that improvements in the magnitude or pattern of the conductance boosts predictive skill scores for strong driving of the system.

To better quantify the variation in model performance, the values of all performance metrics listed in Table 2 were investigated. Table 4 presents these metrics calculated for all model variants at the high dB/dt threshold of 1.5 nT/s. In this table, the results show the *SWPC* configuration in the left and the *Hi-Res SWPC* configuration in the right, with the worst performance by configuration coloured in orange and the best performance coloured in blue. For both the *SWPC* and *Hi-Res SWPC* configurations, the POD and MR improved quite significantly for CMEE and the oval adjustments, indicating that the number of hits and misses increased and decreased, respectively. In addition, all skill score metrics in the latter half of the table, excluding TSS, indicate best performance for CMEE with oval adjustment variant for both resolutions of the model. The TS and F_1 score increased indicating that the number of hits increased. As has been shown in the previous figure and table, the HSS improves as we switch models to introduce oval adjustments and expansion of the dataset. However, the opposite occurred when looking at POFD and FAR values were considered: the application of oval adjustments led to sharply increased FAR values in both low and high res configurations. While the hits and true negatives increased significantly and misses decreased, as supported by the POD and MR values, the number of false alarms increased steadily as the conductance coefficients were changed and jumped significantly with the application of the oval adjustments. This indirectly affected the TSS, which is defined as the difference between the hit rate and miss rate, or mathematically as $1 - (FAR + MR)$. Since the FAR increased, in spite of the decreased MR, TSS values reduced by more than 0.05 as we switched models. Given that this order of change in skill was similar to what was achievable by changing model resolutions, the increment in false alarms is a significant drawback when using oval adjustments. The aforementioned trend was observed in all dB/dt thresholds from 0.7 nT/s and above, indicating that this was not an isolated case. The performance metrics for the other thresholds have been presented in the supp. material.

3.3 Performance Analysis of ΔB Estimation

Unlike the dB/dt performance quantification using binary event analysis, the usage of the same procedure on ΔB values does not help address the science questions posed in Section 1. Figure 10 describes variation in HSS for predicted ΔB from all model variants against observed values. In comparison to the dB/dt predictions, the change in ΔB predictions were not nearly as drastic for better or worse. Note that the y-axis in Figures 10(a) and (b) are not the same as in Figures 9(a) and (b); the HSS range spanned in the case of ΔB is much shorter than in the case of dB/dt . In part (a), the CMEE-driven predictions show deterioration in the HSS values compared to RLM. However, in comparison to the variation in HSS for dB/dt by the expanded dataset, the variation observed is minimal. The decrease in HSS values was similar, but lesser, in the *Hi-Res Set F* results. In part (b), the variation in ΔB HSS values are negligible when oval adjustments were applied, for both model resolutions. In fact, some higher thresholds in part (b) showed no substantial change in the HSS values with the CMEE-driven simulations. When comparing parts (a) and (b) of Figure 10, the HSS values in part (b) are greater than their respective counterpart in part (a) of the figure for thresholds ≥ 200 nT. This indicates that while changing coefficients by increasing the dataset caused more varia-

(a) Impact of Dataset Expansion

Threshold	SWPC Configuration			Hi-Res SWPC Configuration		
	RLM	CMEE	Difference	RLM	CMEE	Difference
0.3 nT/s	0.521	0.554	+0.033	0.624	0.640	+0.016
0.7 nT/s	0.445	0.478	+0.033	0.526	0.559	+0.033
1.1 nT/s	0.353	0.394	+0.040	0.434	0.466	+0.032
1.5 nT/s	0.285	0.312	+0.027	0.330	0.367	+0.037

(b) Effect of Oval Adjustment (OA)

Threshold	SWPC Configuration			Hi-Res SWPC Configuration		
	CMEE	CMEE ⁺	Difference	CMEE	CMEE ⁺	Difference
0.3 nT/s	0.554	0.637	+0.083	0.640	0.685	+0.046
0.7 nT/s	0.478	0.556	+0.078	0.559	0.619	+0.060
1.1 nT/s	0.394	0.474	+0.080	0.466	0.525	+0.059
1.5 nT/s	0.312	0.397	+0.085	0.367	0.465	+0.098

(c) Influence of Dataset expansion and OA Combination

Threshold	SWPC Configuration			Hi-Res SWPC Configuration		
	RLM ⁺	CMEE ⁺	Difference	RLM ⁺	CMEE ⁺	Difference
0.3 nT/s	0.637	0.637	±0.000	0.699	0.685	-0.013
0.7 nT/s	0.498	0.556	+0.058	0.598	0.619	+0.022
1.1 nT/s	0.406	0.474	+0.068	0.492	0.525	+0.033
1.5 nT/s	0.318	0.397	+0.079	0.409	0.465	+0.056

RLM - Empirical Coefficients of the Ridley Legacy Model

CMEE - Empirical Coefficients of the Conductance Model for Extreme Events

RLM⁺ - Ridley Legacy Model, with Auroral Oval AdjustmentsCMEE⁺ - Conductance Model for Extreme Events, with Auroral Oval Adjustments

Table 3. Comparison of Heidke Skill Scores (HSS) for the space weather events listed in Table 1(a) at the prescribed four dB/dt thresholds (leftmost column) from *Pulkkinen2013*. (a) The top-most table compares HSS for the conductance coefficients of RLM and CMEE; no auroral amelioration added to the model; (b) The middle table compares results simulated using the CMEE using only the empirical conductance coefficients, against another version of the model that uses the CMEE coefficients along with the artificial oval adjustments; (c) The bottom-most table compares the two empirical models with the auroral oval adjustments. Here, green signifies improvement, while red signifies deterioration in prediction value.

tion in the HSS values of individual simulation sets, application of oval adjustments improves overall performance regardless of the coefficients used.

For a more quantitative explanation of the ΔB performance, Table 5 presents values of all performance metrics calculated for all model variants at a high ΔB threshold of 400 nT. The table is similarly structured to Table 4 with the worst performance in each configuration coloured orange and the best performance coloured blue. When comparing the coefficient-driven simulations of RLM and CMEE, substantial variations are not observed in almost all skill scores with a maximum difference of ~ 0.02 for any given skill score and resolution. The same is seen with the simulations driven with oval adjustments, which also do not vary substantially. However, a significant jump is observed in the skill scores when comparing the impact of oval adjustments with oval adjusted sim-

ulations performing better than only coefficient-driven simulations. For both low and high res configurations, TS and F₁ skill scores improve when oval adjustments are applied. This is also seen in the accuracy measures like POD and MR whose values improve, with the POD jumping by a value of ~ 0.1 indicating that the number of hits are increasing and number of misses decreasing. Similar to the dB/dt metric analysis and in sharp contrast to the aforementioned performance metrics, the POFD and FAR values are best for simulations driven using non-oval adjustment applications. This is similar to the results in Section 3.2, where false alarms increase as we switch conductance models. Similar to Section 3.2, the trend seen in these performance metrics are not an isolated case for this specific threshold, but observed in all thresholds. The performance metrics for the other thresholds have been presented in the supp. material.

The TSS and HSS do not show substantial differences as the conductance is modified, with the maximum difference between skill scores not being more than ~ 0.05 . By comparison, the difference between the best and the worst HSS performance for the dB/dt is ~ 0.11 . The results also show that the best HSS and TSS for the *Hi-Res* case are simulations driven by RLM coefficients, which is in direct contrast to the low res case where RLM coefficients consistently underperform for both TSS and HSS. This contrast is as a result of using the same time forecast window t_f as the *Pulkkinen2013* on ΔB predictions. The comparison window t_f of 20 minutes, used in both this study and the *Pulkkinen2013* study for dB/dt predictions, is not long enough to observe severe variations in ΔB perturbations. As an example, the predicted ΔB hardly varies over more than two of the pre-determined thresholds, even during strong driving. In comparison, dB/dt varies over multiple thresholds several times within a t_f . This shows that the metrics used in this study are not totally appropriate to study improvements in ΔB predictions. This could simply be done by increasing the comparison time window, or by using different error or bias metrics. As discussed earlier in Section 3.1 estimation of SSPB in Figure 8 for specific magnetometer stations during Event 2 gives a quantitative understanding of the difference.

4 Analysis

The considerable increase in the frequency and magnitude of dB/dt spikes at YKC with the application of the oval adjustments in Figure 7(b) is closely associated to the domain constraints in RIM. As described in Section 2.2.1, while RIM's simulation domain spans the ionosphere pole-to-pole, the empirical auroral conductance module is limited with a spatial domain spanning the poles to MLat 60° . This means that in its present configuration the auroral conductance module, be it RLM or CMEE, is bounded at MLat 60° , with conductance values equatorward of this boundary dropping exponentially and the aurora being constrained poleward of the boundary. The impact of this boundary is clearly indicated in Figure 8(d), where auroral currents are the dominant source of ground ΔB in high latitude regions like YKC, but contribute negligibly at mid latitudinal regions like NEW.

Since application of both the dataset expansion and oval adjustments result in increasing the conductance ceiling during strong driving, CMEE allows more magnetospheric currents to close more dynamically throughout the ionosphere at any given time. In addition, the oval adjustments enhance conductance in regions of high upward FACs thereby changing the pattern of the auroral conductance and reducing the conductance as a function of distance from the empirically constructed oval. The combined effect of these modifications would result in the auroral horizontal currents in RIM's domain being estimated with increased accuracy. This, in turn, leads to a more accurate estimation of the ΔB perturbation and subsequently dB/dt , which are both calculated from the Biot-Savart integral of these current systems (e.g. Yu et al., 2010; Welling, 2019). The conductance modifications due to the two elements (dataset expansion and oval adjustment) lead to noisier results in dB/dt , which leads to increased spikes. These spikes, when correct, in-

Metric	<i>SWPC</i> Configuration				<i>Hi-Res SWPC</i> Configuration			
	RLM	CMEE	RLM ⁺	CMEE ⁺	RLM	CMEE	RLM ⁺	CMEE ⁺
POD	0.2216	0.2490	0.2668	0.3557	0.2791	0.3406	0.4309	0.5554
POFD	0.0169	0.0194	0.0253	0.0319	0.0262	0.0378	0.0566	0.0784
FAR	0.3306	0.3358	0.3810	0.3674	0.3780	0.4182	0.4597	0.4775
MR	0.1089	0.1057	0.1041	0.0932	0.1026	0.0957	0.0852	0.0693
TS	0.1998	0.2211	0.2291	0.2948	0.2386	0.2736	0.3153	0.3684
F1	0.3330	0.3622	0.3728	0.4553	0.3853	0.4297	0.4795	0.5385
TSS	0.5605	0.5585	0.5150	0.5394	0.5194	0.4861	0.4551	0.4532
HSS	0.2855	0.3120	0.3179	0.3973	0.3297	0.3672	0.4094	0.4647

Table 4. Performance metrics table for predicted dB/dt at the 1.5 nT/s threshold. Listed are all performance metrics defined in Table 2 (Leftmost column) measured for SWMF simulations conducted using RLM Coefficients (denoted by 'RLM'), CMEE Coefficients (denoted by 'CMEE'), RLM with oval adjustment (denoted by 'RLM⁺') and CMEE with oval adjustment (denoted by 'CMEE⁺') simulated using both the *SWPC* and *Hi-Res SWPC* configurations. The orange values show the least desirable metric results, while the blue values signify the best results for this threshold.

crease the number of hits and when incorrect, increase the number of false alarms. The emergence of dB/dt spikes in the modeled data during the oval expansion phase in the bottom subplot of Figure 7(b) demarcates why false alarms increase when the oval adjustment factor is used. In addition to the boundary constraints, false alarms are also caused by sudden shifting of the empirically-estimated auroral oval. These shifts are caused as a result of the sensitive dependence of the oval adjustments to changes in FAC patterns. Sharp changes in the FAC occurring over time scales in the same order of the coupling time cadence cause the empirical estimation of the oval to change rapidly. This brisk movement of the placement of the oval adjustment results in the loci movement of dB/dt spikes, causing unexpected hits and/or false alarms. In all, the aforementioned problems place the auroral oval in the wrong spot which lead to dB/dt spikes, perhaps even at the right time, but wrong location hence increasing the false alarms.

While an increment in the number of false alarms is a significant drawback, the advantages of using the improved conductance model in the SWMF far outweigh this issue. Firstly, the expansion of the dataset in CMEE allows for an increased limit cap on the magnitude of the conductance which results in generating a more realistic cross polar cap potential to be fed back as input to the GM and IM modules. This is essential when conducting numerical experiments investigating the magnetosphere-ionosphere coupling. Secondly, the changes in the conductance pattern in CMEE, as a result of the use of nonlinear regression, physically alters the nightside and dayside auroral conductance pattern when compared to RLM. Using global modeling, this numerical experiment has not only been able to address the question of expanded dataset raised by *Welling2017*, but is also able to discern the impact of ionospheric conductance on space weather forecasting. Finally, both the magnitude and pattern of ionospheric conductance proves to be an important quantity in affecting a global model's dB/dt predictive skill. Given that the dB/dt is an important quantity used in the science community and the industry to predict space weather on the ground, accuracy in the ionospheric conductance is important in our global models. Through this work, the authors present an advanced and more accurate auroral conductance model to address this challenge.

Metric	SWPC Configuration				Hi-Res SWPC Configuration			
	RLM	CMEC	RLM ⁺	CMEC ⁺	RLM	CMEC	RLM ⁺	CMEC ⁺
POD	0.4602	0.4385	0.5123	0.5224	0.5687	0.5485	0.6440	0.6671
POFD	0.0575	0.0523	0.0616	0.0658	0.0865	0.0901	0.1393	0.1429
FAR	0.2587	0.2500	0.2516	0.2602	0.2982	0.3146	0.3768	0.3745
MR	0.1701	0.1749	0.1568	0.1546	0.1445	0.1508	0.1289	0.1220
TS	0.3965	0.3826	0.4370	0.4413	0.4580	0.4382	0.4635	0.4767
F1	0.5679	0.5534	0.6082	0.6124	0.6283	0.6093	0.6335	0.6457
TSS	0.5712	0.5751	0.5916	0.5851	0.5573	0.5346	0.4943	0.5035
HSS	0.4585	0.4456	0.5015	0.5042	0.5135	0.4898	0.4994	0.5132

Table 5. Performance metrics table for predicted ΔB at the 400 nT threshold. Listed are all performance metrics defined in Table 2 (Leftmost column) measured for SWMF simulations conducted using the same variants as in Table 4. The orange values show the least desirable metric results, while the blue values signify the best results for this threshold.

5 Conclusion

In this work, the development of an advanced auroral conductance model, CMEC has been presented. CMEC has been designed using nonlinear regression to span minute-resolution data generated from AMIE for the whole year of 2003 spanning extreme events. It has additional capability to add physics-driven empirical adjustments to improve the auroral conductance to ensure a larger range on conductance values to better predict the conductance for a broad range of activity. In this study, this model has been used in the SWMF to investigate the impact of auroral conductance on space weather prediction. Simulated results were compared against observed global quantities like polar cap potential, field aligned current intensity and ground-based magnetic perturbation. Additionally, a quantitative investigation was conducted using a binary event analysis similar to the *Pulkkinen2013* study and skill scores for dB/dt and ΔB predictions were computed.

The investigation showed that application of the increased dataset coupled with oval adjustments led to substantial changes in almost all space weather quantities. CMEC allows the auroral conductance to have an increased range of values, attaining a higher ceiling during extreme driving as compared to RLM. Since FACs are largely driven by upstream conditions, they were not drastically impacted by changes in the conductance model. However, since the conductance value increased and FACs varied minimally, the CPCP values were lowered with the usage of CMEC and the oval adjustments. Since, auroral horizontal currents directly impact the ground magnetic perturbation ΔB and its temporal variant dB/dt , the driving of both these quantities were appreciably altered by the application of both the expanded dataset and oval adjustments. While usage of the expanded dataset resulted in a general increase of the modeled dB/dt magnitude, oval adjustments increased the frequency of dB/dt spikes. Neither of these properties were able to improve the modeling of the auroral oval expansion. This resulted in the formation of different regimes in the latitudinal contribution to the ΔB and dB/dt distributions, with negligible contribution of auroral currents in low or mid latitude magnetometer stations in the modeled output during extreme driving .

The results of the binary event analysis conducted on the simulation variants indicated that usage of CMEC with oval adjustments yields best performance, with drastic improvements in the HSS metric at higher activity thresholds. In addition, most performance metrics exhibited favourable changes when applying the CMEC coefficients and/or oval adjustments, indicating an increase in the number of identified hits and true neg-

807 atives and a decrease in misses. However, the performance metrics also indicated that
 808 the number of false alarms increased with the application of the oval adjustment. This
 809 was caused predominantly because of the brisk movement of the empirically-estimated
 810 oval, and the latitudinal constraint on the auroral conductance which inhibits the oval
 811 from expanding beyond MLat 60°, thereby pushing the auroral currents poleward. While
 812 this process increases the number of hits, favourably affecting most performance met-
 813 rics, it also hurts metrics like TSS due to increased number of false alarms. The binary
 814 event analysis of ΔB predictions do not yield definitive results, exhibiting minimal im-
 815 pact on skill scores. This is most likely because the time forecast window of 20 minutes,
 816 chosen to study dB/dt forecasts in the original *Pulkkinen2013* study, is limited for the
 817 ΔB to exhibit significant change in value so as to jump multiple number of thresholds
 818 and therefore produce any meaningful changes in the performance metrics. Outstand-
 819 ing shortcomings of the present analysis such as those mentioned above and additional
 820 analysis like estimation of bias and error metrics for various thresholds are steps that
 821 we are presently pursuing. Because validation is a process, continued data-model com-
 822 parisons will be performed in future studies.

823 The issues causing the misidentification of dB/dt spikes requires a physical solu-
 824 tion with numerical modifications to allow the aurora to expand to mid or low latitudes
 825 during extreme events. While this could be done with data, an easier and more novel
 826 solution would be to drive precipitation from the magnetospheric domains. This could
 827 be done by coupling physics-based precipitative inputs from GM and IM modules to es-
 828 timate electron and ion precipitation in the aurora. This is similar to what has been done
 829 in studies like Raeder et al. (2001) and Wiltberger et al. (2001). Such an approach al-
 830 lows for a novel approach to isolate and understand the impact of individual sources of
 831 auroral conductance. At the same time, the precipitation pattern of the aurora allows
 832 observational data from extreme events to feature prominently in perceiving the accu-
 833 racy of precipitative fluxes at different MLTs and magnetic latitudes. The development
 834 of such a model is presently being undertaken by the authors to address the aforemen-
 835 tioned issue (Mukhopadhyay et al., 2018, 2019).

836 In conclusion, the usage of CMEE designed using an increased dataset coupled with
 837 the application of oval adjustment parameters lead to substantial changes in our dB/dt
 838 predictions. With the crucial impact that the auroral conductance imparts on global quan-
 839 tities, CMEE would serve as a competent replacement to RLM's coefficient map. The
 840 usage of the oval adjustments in the SWMF's auroral conductance estimation is unique
 841 and compelling in driving future developments of auroral conductance models to achieve
 842 accuracy in the conductance pattern, in addition to the magnitude. Additionally, as ev-
 843 idenced by the skill score analysis, the new model leads to significant improvement in
 844 predictive skill of our space weather model.

845 Acknowledgments

846 Support for this work has been provided by NASA Grants NNX17AB87G, 80NSSC18K1120,
 847 and 80NSSC17K0015, and NSF Grant 1663770. We would like to acknowledge high-performance
 848 computing support from Pleiades (allocation 1815) provided by NASA's High-End Com-
 849 puting Capability Programme, and Cheyenne (allocation UUSL0016) provided by NCAR's
 850 Computational and Information Systems Laboratory, sponsored by the National Science
 851 Foundation. Model result data, input files and observation data are available via <https://doi.org/10.7302/nwxp-g551>. The Space Weather Modeling Framework is maintained by the University of Michigan
 852 Center for Space Environment Modeling and can be obtained at <http://csem.engin.umich.edu/tools/swmf>.
 853 AMIE Results used in this study are maintained at the University of Michigan's Virtual
 854 Model Repository (VMR; <http://vmr.engin.umich.edu/>) by AJR.

855 The authors would like to thank Dr. Meghan Burleigh for reading a draft manuscript.
 856 We thank Dr. Shasha Zou, Dr. Robert Robinson, Dr. Steven Morley and Dr. Gabor Toth
 857 for sharing their expertise in the course of this study. A.M. would like to thank Dr. Do-

859 gacan su Ozturk, Dr. Zhenguang Huang, Dr. Natalia Ganjushkina, Ms. Abigail Azari,
 860 Mr. Alexander Shane, Mr. Brian Swiger and Mr. Christopher Bert for sharing their ex-
 861 pertise during the development of modeling, curve-fitting and validation tools used in
 862 this study.

863 References

- 864 Ahn, B.-H., Richmond, A. D., Kamide, Y., Kroehl, H. W., Emery, B. A., de la
 865 Beaujardié, O., & Akasofu, S.-I. (1998, jul). An ionospheric conduc-
 866 tance model based on ground magnetic disturbance data. *Journal of Geo-*
 867 *physical Research: Space Physics*, 103(A7), 14769–14780. Retrieved from
 868 <http://doi.wiley.com/10.1029/97JA03088> doi: 10.1029/97JA03088
- 869 Anderson, B. J., Korth, H., Waters, C. L., Green, D. L., Merkin, V. G., Barnes,
 870 R. J., & Dyrud, L. P. (2014). Development of large-scale birkeland currents de-
 871 termined from the active magnetosphere and planetary electrodynamics response
 872 experiment. *Geophysical Research Letters*, 41(9), 3017–3025. Retrieved from
 873 <https://agupubs.onlinelibrary.wiley.com/doi/abs/10.1002/2014GL059941>
 874 doi: 10.1002/2014GL059941
- 875 Anderson, B. J., Korth, H., Welling, D. T., Merkin, V. G., Wiltberger, M. J.,
 876 Raeder, J., ... Rastaetter, L. (2017). Comparison of predictive estimates of
 877 high-latitude electrodynamics with observations of global-scale birkeland currents.
 878 *Space Weather*, 15(2), 352–373. Retrieved from <https://agupubs.onlinelibrary.wiley.com/doi/abs/10.1002/2016SW001529> doi: 10.1002/2016SW001529
- 879 Axford, W. I., & Hines, C. O. (1961). A Unifying Theory of High-Latitude Geophys-
 880 ical Phenomena and Geomagnetic Storms. *Canadian Journal of Physics*, 39(10),
 881 1433–1464. Retrieved from <https://doi.org/10.1139/p61-172> doi: 10.1139/
 882 p61-172
- 883 Boonsiriseth, A., Thorne, R. M., Lu, G., Jordanova, V. K., Thomsen, M. F., Ober,
 884 D. M., & Ridley, A. J. (2001, jul). A semiempirical equatorial mapping of
 885 AMIE convection electric potentials (MACEP) for the January 10, 1997, mag-
 886 netic storm. *Journal of Geophysical Research: Space Physics*, 106(A7), 12903–
 887 12917. Retrieved from <http://doi.wiley.com/10.1029/1999JA000332> doi:
 888 10.1029/1999JA000332
- 889 Brekke, A., & Moen, J. (1993). Observations of high latitude ionospheric con-
 890 ductances. *Journal of Atmospheric and Terrestrial Physics*, 55(11), 1493–
 891 1512. Retrieved from <http://www.sciencedirect.com/science/article/pii/002191699390126J> doi: [https://doi.org/10.1016/0021-9169\(93\)90126-J](https://doi.org/10.1016/0021-9169(93)90126-J)
- 892 Carter, J. A., Milan, S. E., Coxon, J. C., Walach, M.-T., & Anderson, B. J. (2016).
 893 Average field-aligned current configuration parameterized by solar wind con-
 894 ditions. *Journal of Geophysical Research: Space Physics*, 121(2), 1294–1307.
 895 Retrieved from <https://agupubs.onlinelibrary.wiley.com/doi/abs/10.1002/2015JA021567> doi: 10.1002/2015JA021567
- 896 Chapman, S. (1931, jan). The absorption and dissociative or ionizing effect of
 897 monochromatic radiation in an atmosphere on a rotating earth. *Proceedings of
 898 the Physical Society*, 43(1), 26–45. Retrieved from <http://stacks.iop.org/0959-5309/43/i=1/a=305?key=crossref.46895a3aef390982dcfb99f7afc88ced>
 899 doi: 10.1088/0959-5309/43/1/305
- 900 Cid, C., Saiz, E., Guerrero, A., Palacios, J., & Cerrato, Y. (2015). A Carrington-like
 901 geomagnetic storm observed in the 21st century. *J. Space Weather Space Clim.*, 5,
 902 A16. Retrieved from <https://doi.org/10.1051/swsc/2015017> doi: 10.1051/
 903 swsc/2015017
- 904 Connor, H. K., Zesta, E., Fedrizzi, M., Shi, Y., Raeder, J., Codrescu, M. V., &
 905 Fuller-Rowell, T. J. (2016). Modeling the ionosphere-thermosphere response
 906 to a geomagnetic storm using physics-based magnetospheric energy input:

- 911 OpenGGCM-CTIM results. *Journal of Space Weather and Space Climate*, 6,
 912 A25. Retrieved from <http://www.swsc-journal.org/10.1051/swsc/2016019>
 913 doi: 10.1051/swsc/2016019
- 914 De Zeeuw, D. L., Sazykin, S., Wolf, R. A., Gombosi, T. I., Ridley, A. J., & Tóth,
 915 G. (2004). Coupling of a global MHD code and an inner magnetospheric model:
 916 Initial results. *Journal of Geophysical Research: Space Physics*, 109(A12), 1–14.
 917 doi: 10.1029/2003JA010366
- 918 Dungey, J. W. (1963, jan). Interactions of solar plasma with the geomag-
 919 netic field. *Planetary and Space Science*, 10, 233–237. Retrieved from
 920 <https://www.sciencedirect.com/science/article/pii/0032063363900205>
 921 doi: 10.1016/0032-0633(63)90020-5
- 922 Frahm, R. A., Winningham, J. D., Sharber, J. R., Link, R., Crowley, G., Gaines,
 923 E. E., ... Potemra, T. A. (1997, dec). The diffuse aurora: A significant source
 924 of ionization in the middle atmosphere. *Journal of Geophysical Research: At-*
925 mospheres, 102(D23), 28203–28214. Retrieved from <http://doi.wiley.com/10.1029/97JD02430> doi: 10.1029/97JD02430
- 926 Fuller-Rowell, T. J., & Evans, D. S. (1987). Height-integrated pedersen and hall
 927 conductivity patterns inferred from the tiros-noaa satellite data. *Journal of Geo-*
928 physical Research: Space Physics, 92(A7), 7606–7618. Retrieved from <https://agupubs.onlinelibrary.wiley.com/doi/abs/10.1029/JA092iA07p07606> doi:
 931 10.1029/JA092iA07p07606
- 932 Gao, Y. (2012). Comparing the cross polar cap potentials measured by superdarn
 933 and amie during saturation intervals. *Journal of Geophysical Research: Space*
934 Physics, 117(A8). Retrieved from <https://agupubs.onlinelibrary.wiley.com/doi/abs/10.1029/2012JA017690> doi: 10.1029/2012JA017690
- 935 Glocer, A., Rastatter, L., Kuznetsova, M., Pulkkinen, A., Singer, H. J., Balch, C., ...
 936 Wing, S. (2016). Community-wide validation of geospace model local k-index
 937 predictions to support model transition to operations. *Space Weather*, 14(7),
 938 469–480. Retrieved from <https://agupubs.onlinelibrary.wiley.com/doi/abs/10.1002/2016SW001387> doi: 10.1002/2016SW001387
- 939 Gombosi, T. I., De Zeeuw, D. L., Powell, K. G., Ridley, A. J., Sokolov, I. V., Stout,
 940 Q. F., & Tóth, G. (2003). Adaptive mesh refinement for global magnetohydrodynamic
 941 simulation. In J. Büchner, M. Scholer, & C. T. Dum (Eds.), *Space*
942 plasma simulation (pp. 247–274). Berlin, Heidelberg: Springer Berlin Heidelberg.
 943 Retrieved from https://doi.org/10.1007/3-540-36530-3_12 doi:
 944 10.1007/3-540-36530-3_12
- 945 Goodman, M. L. (1995, aug). A three-dimensional, iterative mapping procedure
 946 for the implementation of an ionosphere-magnetosphere anisotropic Ohm's law
 947 boundary condition in global magnetohydrodynamic simulations. *Annales*
948 Geophysicae, 13(8), 843–853. Retrieved from <https://doi.org/10.1007/s00585-995-0843-z> doi: 10.1007/s00585-995-0843-z
- 949 Haiducek, J. D., Welling, D. T., Ganushkina, N. Y., Morley, S. K., & Ozturk, D. S.
 950 (2017). SWMF Global Magnetosphere Simulations of January 2005: Geomagnetic
 951 Indices and Cross-Polar Cap Potential. *Space Weather*, 15(12), 1567–1587. Re-
 952 tried from <https://agupubs.onlinelibrary.wiley.com/doi/abs/10.1002/2017SW001695> doi: 10.1002/2017SW001695
- 953 Hanssen, A. W., & Kuipers, W. J. A. (1965). On the relationship between the fre-
 954 quency of rain and various meteorological parameters. *Meded. Verh.*, 81, 2 – 15.
- 955 Heidke, P. (1926). Berechnung des Erfolges und der Güte der
 956 Windstärkevorhersagen im Sturmwarnungsdienst. *Geografiska Annaler*, 8, 301–
 957 349.
- 958 Herrmann, L. R. (1976). Laplacian-Isoparametric Grid Generation Scheme. *Journal*
959 of the Engineering Mechanics Division, 102(5), 749–907.
- 960 Honkonen, I., Rastätter, L., Grocott, A., Pulkkinen, A., Palmroth, M., Raeder,

- 965 J., ... Wiltberger, M. (2013, may). On the performance of global magnetohydrodynamic models in the Earth's magnetosphere. *Space Weather*, 11(5),
 966 313–326. Retrieved from <http://doi.wiley.com/10.1002/swe.20055> doi:
 967 10.1002/swe.20055
- 968 Iijima, T., & Potemra, T. A. (1976). The amplitude distribution of field-aligned currents at northern high latitudes observed by Triad. *Journal of Geophysical Research-Space Physics*, 81(13), 2165–2174. Retrieved from <http://onlinelibrary.wiley.com/doi/10.1029/JA081i013p02165/abstract> doi:10.1029/JA081i013p02165
- 969 Jolliffe, I. T., & Stephenson, D. B. (2012). *Forecast Verification: A Practitioner's Guide in Atmospheric Science*. John Wiley & Sons. Retrieved from <https://books.google.com/books?hl=en&lr={&}id=DCxsKQeaBH8C&pgis=1>
- 970 Khachikyan, G. Y., Koustov, A. V., & Sofko, G. J. (2008). Dependence of super-darn cross polar cap potential upon the solar wind electric field and magnetopause subsolar distance. *Journal of Geophysical Research: Space Physics*, 113(A9). Retrieved from <https://agupubs.onlinelibrary.wiley.com/doi/abs/10.1029/2008JA013107> doi: 10.1029/2008JA013107
- 971 Kihm, E. A., & Ridley, A. J. (2005). A statistical analysis of the assimilative mapping of ionospheric electrodynamics auroral specification. *Journal of Geophysical Research: Space Physics*, 110(A7). Retrieved from <https://agupubs.onlinelibrary.wiley.com/doi/abs/10.1029/2003JA010371> doi: 10.1029/2003JA010371
- 972 Knight, S. (1973). Parallel electric fields. *Planetary and Space Science*. doi: 10.1016/0032-0633(73)90093-7
- 973 Korth, H., Zhang, Y., Anderson, B. J., Sotirelis, T., & Waters, C. L. (2014). Statistical relationship between large-scale upward field-aligned currents and electron precipitation. *Journal of Geophysical Research: Space Physics*, 119(8), 6715–6731. Retrieved from <https://agupubs.onlinelibrary.wiley.com/doi/abs/10.1002/2014JA019961> doi: 10.1002/2014JA019961
- 974 Le, G., Lhr, H., Anderson, B. J., Strangeway, R. J., Russell, C. T., Singer, H., ...
 975 Torbert, R. B. (2016). Magnetopause erosion during the 17 march 2015 magnetic storm: Combined field-aligned currents, auroral oval, and magnetopause observations. *Geophysical Research Letters*, 43(6), 2396-2404. Retrieved from <https://agupubs.onlinelibrary.wiley.com/doi/abs/10.1002/2016GL068257> doi: 10.1002/2016GL068257
- 976 Liemohn, M. W., Ganushkina, N. Y., De Zeeuw, D. L., Rastaetter, L., Kuznetsova, M., Welling, D. T., ... van der Holst, B. (2018). Real-time swmf at ccmc: Assessing the dst output from continuous operational simulations. *Space Weather*, 16(10), 1583-1603. Retrieved from <https://agupubs.onlinelibrary.wiley.com/doi/abs/10.1029/2018SW001953> doi: 10.1029/2018SW001953
- 977 Liemohn, M. W., McCollough, J. P., Jordanova, V. K., Ngwira, C. M., Morley, S. K., Cid, C., ... Vasile, R. (2018). Model evaluation guidelines for geomagnetic index predictions. *Space Weather*, 16(12), 2079-2102. Retrieved from <https://agupubs.onlinelibrary.wiley.com/doi/abs/10.1029/2018SW002067> doi: 10.1029/2018SW002067
- 978 Liemohn, M. W., Ridley, A. J., Brandt, P. C., Gallagher, D. L., Kozyra, J. U., Ober, D. M., ... DeMajistre, R. (2005, dec). Parametric analysis of nightside conductance effects on inner magnetospheric dynamics for the 17 April 2002 storm. *Journal of Geophysical Research*, 110(A12), A12S22. Retrieved from <http://doi.wiley.com/10.1029/2005JA011109> doi: 10.1029/2005JA011109
- 979 Lu, G., Siscoe, G. L., Richmond, A. D., Pulkkinen, T. I., Tsyganenko, N. A.,
 980 Singer, H. J., & Emery, B. A. (1997). Mapping of the ionospheric field-aligned currents to the equatorial magnetosphere. *Journal of Geophysical*

- 1019 Research: Space Physics, 102(A7), 14467–14476. Retrieved from <https://agupubs.onlinelibrary.wiley.com/doi/abs/10.1029/97JA00744> doi: 10.1029/97JA00744

1020 Merkin, V. G., Milikh, G., Papadopoulos, K., Lyon, J., Dimant, Y. S., Sharma,
1021 A. S., ... Wiltberger, M. (2005, nov). Effect of anomalous electron heating on
1022 the transpolar potential in the LFM global MHD model. *Geophysical Research
1023 Letters*, 32(22), n/a–n/a. Retrieved from <http://doi.wiley.com/10.1029/2005GL023315> doi: 10.1029/2005GL023315

1024 Merkin, V. G., Sharma, A. S., Papadopoulos, K., Milikh, G., Lyon, J., & Goodrich,
1025 C. (2005, sep). Global MHD simulations of the strongly driven magnetosphere:
1026 Modeling of the transpolar potential saturation. *Journal of Geophysical Research:
1027 Space Physics*, 110(A9). Retrieved from <http://doi.wiley.com/10.1029/2004JA010993> doi: 10.1029/2004JA010993

1028 Merkine, V. G., Papadopoulos, K., Milikh, G., Sharma, A. S., Shao, X., Lyon, J.,
1029 & Goodrich, C. (2003, dec). Effects of the solar wind electric field and iono-
1030 spheric conductance on the cross polar cap potential: Results of global MHD
1031 modeling. *Geophysical Research Letters*, 30(23), n/a–n/a. Retrieved from
1032 <http://doi.wiley.com/10.1029/2003GL017903> doi: 10.1029/2003GL017903

1033 Moen, J., & Brekke, A. (1993, may). The solar flux influence on quiet time con-
1034 ductances in the auroral ionosphere. *Geophysical Research Letters*, 20(10), 971–
1035 974. Retrieved from <http://doi.wiley.com/10.1029/92GL02109> doi: 10.1029/92GL02109

1036 Morley, S. K., Brito, T. V., & Welling, D. T. (2018). Measures of Model Per-
1037 formance Based On the Log Accuracy Ratio. *Space Weather*, 16(1), 69–88. Re-
1038 tried from <https://agupubs.onlinelibrary.wiley.com/doi/abs/10.1002/2017SW001669> doi: 10.1002/2017SW001669

1039 Mukhopadhyay, A. (2017). *Statistical Comparison of Magnetopause Distances and
1040 CPCP Estimation by Global MHD Models* (Tech. Rep.). Retrieved from <https://ccmc.gsfc.nasa.gov/RoR{ }WWW/SWREDI/contest-presentations/2017/Statistical{ }Comparison{ }of{ }MP{ }Distances{ }and{ }CPCP{ }CCMC{ }Contest{ }2{ }AgnitM.pdf> doi: <https://doi.org/10.1002/essoar.10502157.1>

1041 Mukhopadhyay, A., Welling, D., Burleigh, M., Ridley, A., Liemohn, M., Anderson,
1042 B., & Gjerloev, J. (2019, dec). Conductance in the Aurora: Influence of Magneto-
1043 spheric Contributors. In *Agu fall meeting abstracts* (Vol. 2019, pp. SA41B–3169).
1044 Retrieved from <https://ui.adsabs.harvard.edu/abs/2019AGUFMSA41B3169M/abstract> doi: doi.org/10.1002/essoar.10502150.1

1045 Mukhopadhyay, A., Welling, D., Liemohn, M., Zou, S., & Ridley, A. (2018, dec).
1046 Challenges in Space Weather Prediction: Estimation of Auroral Conductance.
1047 In *Agu fall meeting abstracts* (Vol. 2018, pp. SA33B–3462). Retrieved from
1048 <https://ui.adsabs.harvard.edu/abs/2018AGUFMSA33B3462M/abstract>

1049 Newell, P. T., Sotirelis, T., & Wing, S. (2009, sep). Diffuse, monoenergetic, and
1050 broadband aurora: The global precipitation budget. *Journal of Geophysical
1051 Research: Space Physics*, 114(A9). Retrieved from <http://doi.wiley.com/10.1029/2009JA014326> doi: 10.1029/2009JA014326

1052 Ohtani, S., Wing, S., Merkin, V. G., & Higuchi, T. (2014, jan). Solar cycle
1053 dependence of nightside field-aligned currents: Effects of dayside ionospheric
1054 conductivity on the solar wind-magnetosphere-ionosphere coupling. *Journal
1055 of Geophysical Research: Space Physics*, 119(1), 322–334. Retrieved from
1056 <http://doi.wiley.com/10.1002/2013JA019410> doi: 10.1002/2013JA019410

1057 Ozturk, D. S., Zou, S., & Slavin, J. A. (2017). IMF By effects on ground mag-
1058 netometer response to increased solar wind dynamic pressure derived from
1059 global MHD simulations. *Journal of Geophysical Research: Space Physics*. doi:
1060 10.1002/2017JA023903

1061 Perlongo, N. J., Ridley, A. J., Liemohn, M. W., & Katus, R. M. (2017, apr). The
1062

- 1073 effect of ring current electron scattering rates on magnetosphere-ionosphere
 1074 coupling. *Journal of Geophysical Research: Space Physics*, 122(4), 4168–
 1075 4189. Retrieved from <http://doi.wiley.com/10.1002/2016JA023679> doi:
 1076 10.1002/2016JA023679
- 1077 Powell, K. G., Roe, P. L., Linde, T. J., Gombosi, T. I., & Zeeuw, D. L. D.
 1078 (1999). A Solution-Adaptive Upwind Scheme for Ideal Magnetohydrodynamics.
 1079 *Journal of Computational Physics*, 154(2), 284–309. Retrieved from
 1080 <http://www.sciencedirect.com/science/article/pii/S002199919996299X>
 1081 doi: <https://doi.org/10.1006/jcph.1999.6299>
- 1082 Pujol, J. (2007). The solution of nonlinear inverse problems and the Levenberg-
 1083 Marquardt method. *Geophysics*, 72(4), W1–W16. Retrieved from <https://doi.org/10.1190/1.2732552> doi: 10.1190/1.2732552
- 1085 Pulkkinen, A., Kuznetsova, M., Ridley, A., Raeder, J., Vapirev, A., Weimer, D., ...
 1086 Chulaki, A. (2011, feb). Geospace Environment Modeling 2008–2009
 1087 Challenge: Ground magnetic field perturbations. *Space Weather*, 9(2), n/a–
 1088 n/a. Retrieved from <http://doi.wiley.com/10.1029/2010SW000600> doi:
 1089 10.1029/2010SW000600
- 1090 Pulkkinen, A., Rastätter, L., Kuznetsova, M., Singer, H., Balch, C., Weimer, D., ...
 1091 Weigel, R. (2013, jun). Community-wide validation of geospace model ground
 1092 magnetic field perturbation predictions to support model transition to opera-
 1093 tions. *Space Weather*, 11(6), 369–385. Retrieved from <http://doi.wiley.com/10.1002/swe.20056> doi: 10.1002/swe.20056
- 1095 Raeder, J., McPherron, R. L., Frank, L. A., Kokubun, S., Lu, G., Mukai, T., ...
 1096 Slavin, J. A. (2001). Global simulation of the Geospace Environment Model-
 1097 ing substorm challenge event. *Journal of Geophysical Research-Space Physics*,
 1098 106(A1), 381–395. doi: 10.1029/2000ja000605
- 1099 Richmond, A. D., & Kamide, Y. (1988). Mapping electrodynamic features of the
 1100 high-latitude ionosphere from localized observations - Technique. *Journal of Geo-
 1101 physical Research*, 93(A6), 5741–5759. doi: 10.1029/JA093iA06p05741
- 1102 Ridley, A. J., De Zeeuw, D. L., Gombosi, T. I., & Powell, K. G. (2001). Using
 1103 steady state MHD results to predict the global state of the magnetosphere-
 1104 ionosphere system. *Journal of Geophysical Research*, 106(A12), 30067. Re-
 1105 tried from <http://adsabs.harvard.edu/abs/2001JGR...10630067R> doi:
 1106 10.1029/2000JA002233
- 1107 Ridley, A. J., Gombosi, T. I., & De Zeeuw, D. L. (2004). Ionospheric control of the
 1108 magnetosphere: conductance. *Annales Geophysicae*, 22(2), 567–584. Retrieved
 1109 from <https://hal.archives-ouvertes.fr/hal-00317238/> doi: 10.5194/angeo-
 1110 -22-567-2004
- 1111 Ridley, A. J., & Liemohn, M. W. (2002, aug). A model-derived storm time
 1112 asymmetric ring current driven electric field description. *Journal of Geophys-
 1113 ical Research: Space Physics*, 107(A8), SMP 2–1–SMP 2–12. Retrieved from
 1114 <http://doi.wiley.com/10.1029/2001JA000051> doi: 10.1029/2001JA000051
- 1115 Robinson, R. M., Vondrak, R. R., Miller, K., Dabbs, T., & Hardy, D. (1987,
 1116 mar). On calculating ionospheric conductances from the flux and energy
 1117 of precipitating electrons. *Journal of Geophysical Research*, 92(A3), 2565.
 1118 Retrieved from <http://doi.wiley.com/10.1029/JA092iA03p02565> doi:
 1119 10.1029/JA092iA03p02565
- 1120 Robinson, R. M., Zhang, Y., Anderson, B. J., Zanetti, L. J., Korth, H., & Fitzmaur-
 1121 rice, A. (2018). Statistical relations between field-aligned currents and precip-
 1122 itating electron energy flux. *Geophysical Research Letters*, 45(17), 8738–8745.
 1123 Retrieved from <https://agupubs.onlinelibrary.wiley.com/doi/abs/10.1029/2018GL078718> doi: 10.1029/2018GL078718
- 1125 Roederer, J. G. (1970). *Dynamics of Geomagnetically Trapped Radiation* (Vol. 2).
 1126 Berlin, Heidelberg: Springer Berlin Heidelberg. doi: <https://doi.org/10.1007/978-3>

- 1127 -642-49300-3
- 1128 Schunk, R., & Nagy, A. (2009). *Ionospheres: Physics, Plasma Physics, and Chemistry* (2nd ed.). Cambridge University Press. doi: 10.1017/CBO9780511635342
- 1129 Sorkine, O., Cohen-Or, D., Lipman, Y., Alexa, M., Rössl, C., & Seidel, H.-P. (2004).
1130 Laplacian surface editing. In *Proceedings of the 2004 eurographics/acm siggraph*
1131 *symposium on geometry processing* (p. 175184). New York, NY, USA: Association
1132 for Computing Machinery.
1133 Retrieved from <https://doi.org/10.1145/1057432.1057456> doi: 10.1145/1057432.1057456
- 1134 Tóth, G., Meng, X., Gombosi, T. I., & Rastäetter, L. (2014). Predicting the time
1135 derivative of local magnetic perturbations. *Journal of Geophysical Research: Space*
1136 *Physics*, 119(1), 310–321.
1137 Retrieved from <https://agupubs.onlinelibrary.wiley.com/doi/abs/10.1002/2013JA019456> doi: 10.1002/2013JA019456
- 1138 Tóth, G., Sokolov, I. V., Gombosi, T. I., Chesney, D. R., Clauer, C. R., De Zeeuw,
1139 D. L., ... Kóta, J. (2005, dec). Space Weather Modeling Framework: A new tool
1140 for the space science community. *Journal of Geophysical Research*, 110(A12),
1141 A12226.
1142 Retrieved from <http://doi.wiley.com/10.1029/2005JA011126> doi:
1143 10.1029/2005JA011126
- 1144 Tóth, G., van der Holst, B., Sokolov, I. V., De Zeeuw, D. L., Gombosi, T. I.,
1145 Fang, F., ... Opher, M. (2012). Adaptive numerical algorithms in space
1146 weather modeling. *Journal of Computational Physics*, 231(3), 870–903.
1147 doi: 10.1016/j.jcp.2011.02.006
- 1148 Waters, C. L., Anderson, B. J., Green, D. L., Korth, H., Barnes, R. J., & Van-
1149 hamäki, H. (2020). Science data products for ampere. In M. W. Dunlop &
1150 H. Lühr (Eds.), *Ionospheric multi-spacecraft analysis tools: Approaches for de-*
1151 *riving ionospheric parameters* (pp. 141–165). Cham: Springer International
1152 Publishing.
1153 Retrieved from https://doi.org/10.1007/978-3-030-26732-2_7 doi: 10.1007/978-3-030-26732-2_7
- 1154 Welling, D. T. (2019). Magnetohydrodynamic models of b and their use in gic
1155 estimates. In *Geomagnetically induced currents from the sun to the power grid*
1156 (p. 43-65). American Geophysical Union (AGU).
1157 Retrieved from <https://agupubs.onlinelibrary.wiley.com/doi/abs/10.1002/9781119434412.ch3>
1158 doi: 10.1002/9781119434412.ch3
- 1159 Welling, D. T., Anderson, B. J., Crowley, G., Pulkkinen, A. A., & Rastäetter, L.
1160 (2017, jan). Exploring predictive performance: A reanalysis of the geospace
1161 model transition challenge. *Space Weather*, 15(1), 192–203.
1162 Retrieved from <http://doi.wiley.com/10.1002/2016SW001505> doi: 10.1002/2016SW001505
- 1163 Welling, D. T., Ngwira, C. M., Opgenoorth, H., Haidukek, J. D., Savani, N. P.,
1164 Morley, S. K., ... Liemohn, M. (2018). Recommendations for next-generation
1165 ground magnetic perturbation validation. *Space Weather*, 16(12), 1912-1920.
1166 Retrieved from <https://agupubs.onlinelibrary.wiley.com/doi/abs/10.1029/2018SW002064> doi: 10.1029/2018SW002064
- 1167 Welling, D. T., & Ridley, A. J. (2010). Exploring sources of magnetospheric plasma
1168 using multispecies MHD. *Journal of Geophysical Research: Space Physics*,
1169 115(A4).
1170 Retrieved from <https://agupubs.onlinelibrary.wiley.com/doi/abs/10.1029/2009JA014596> doi: 10.1029/2009JA014596
- 1171 Wilks, D. S. (2011). *Statistical methods in the atmospheric sciences* (3rd ed.). Academic Press.
- 1172 Wiltberger, M., Merkin, V., Zhang, B., Toftoletto, F., Oppenheim, M., Wang,
1173 W., ... Stephens, G. K. (2017, may). Effects of electrojet turbulence on
1174 a magnetosphere-ionosphere simulation of a geomagnetic storm. *Journal of*
1175 *Geophysical Research: Space Physics*, 122(5), 5008–5027.
1176 Retrieved from <http://doi.wiley.com/10.1002/2016JA023700> doi: 10.1002/2016JA023700
- 1177 Wiltberger, M., Wang, W., Burns, A. G., Solomon, S. C., Lyon, J. G., & Goodrich,
1178 C. C. (2004). Initial results from the coupled magnetosphere ionosphere ther-

- mosphere model: magnetospheric and ionospheric responses. *Journal of Atmospheric and Solar-Terrestrial Physics*, 66(15), 1411–1423. Retrieved from <http://www.sciencedirect.com/science/article/pii/S136468260400149X> doi: <https://doi.org/10.1016/j.jastp.2004.03.026>
- Wiltberger, M., Weigel, R. S., Lotko, W., & Fedder, J. A. (2001). Modeling seasonal variations of auroral particle precipitation in a global-scale magnetosphere-ionosphere simulation. *Journal of Geophysical Research-Space Physics*, 114(A1), 381–395. doi: 10.1029/2008JA013108
- Wolf, R. A., Harel, M., Spiro, R. W., Voigt, G.-H., Reiff, P. H., & Chen, C.-K. (1982, aug). Computer simulation of inner magnetospheric dynamics for the magnetic storm of July 29, 1977. *Journal of Geophysical Research*, 87(A8), 5949. Retrieved from <http://doi.wiley.com/10.1029/JA087iA08p05949> doi: 10.1029/JA087iA08p05949
- Yagou, H., Ohtake, Y., & Belyaev, A. (2002, July). Mesh smoothing via mean and median filtering applied to face normals. In *Geometric modeling and processing. theory and applications. gmp 2002. proceedings* (p. 124-131). doi: 10.1109/GMAP.2002.1027503
- Yu, Y., Jordanova, V. K., Ridley, A. J., Albert, J. M., Horne, R. B., & Jeffery, C. A. (2016). A new ionospheric electron precipitation module coupled with ram-scb within the geospace general circulation model. *Journal of Geophysical Research: Space Physics*, 121(9), 8554–8575. Retrieved from <https://agupubs.onlinelibrary.wiley.com/doi/abs/10.1002/2016JA022585> doi: 10.1002/2016JA022585
- Yu, Y., Ridley, A. J., Welling, D. T., & Tóth, G. (2010, aug). Including gap region field-aligned currents and magnetospheric currents in the MHD calculation of ground-based magnetic field perturbations. *Journal of Geophysical Research: Space Physics*, 115(A8). Retrieved from <http://doi.wiley.com/10.1029/2009JA014869> doi: 10.1029/2009JA014869
- Zhang, B., Lotko, W., Brambles, O., Wiltberger, M., & Lyon, J. (2015). Electron precipitation models in global magnetosphere simulations. *Journal of Geophysical Research: Space Physics*, 120(2), 1035–1056. Retrieved from <https://agupubs.onlinelibrary.wiley.com/doi/abs/10.1002/2014JA020615> doi: 10.1002/2014JA020615

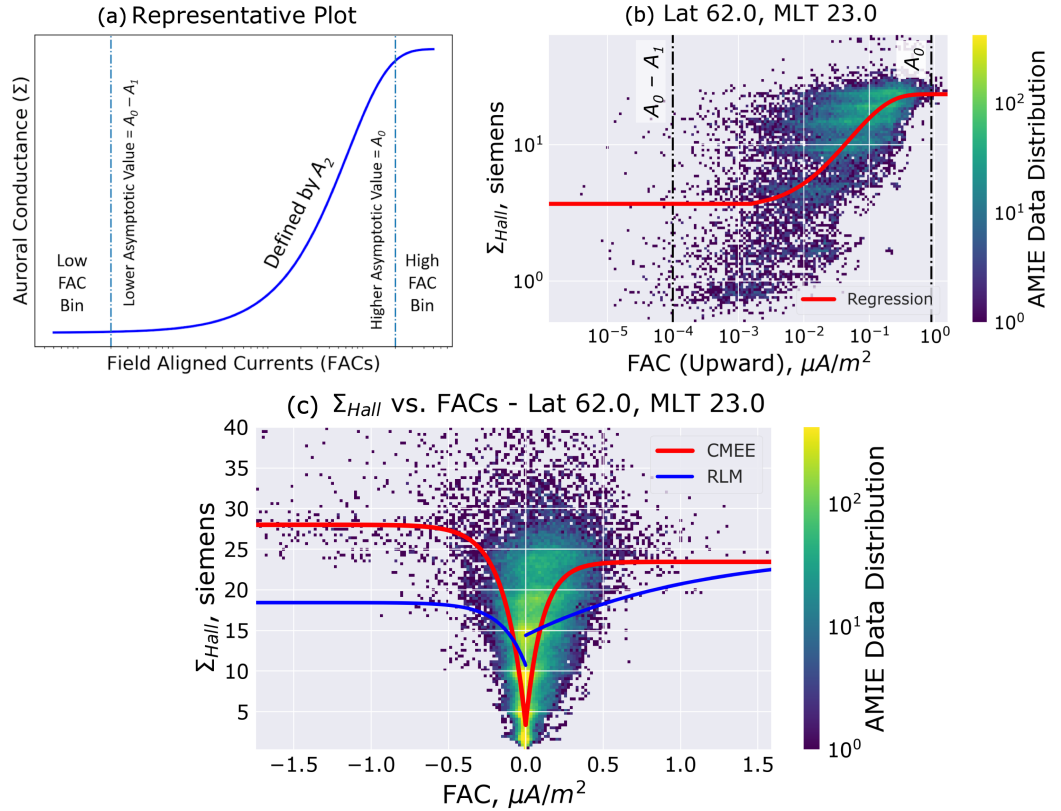


Figure 3. Example Fitting of the Conductance Model for Extreme Events (CMEE) - (a) Representative Line Plot of Auroral Conductance (Hall or Pedersen, in siemens) vs. Field Aligned Currents (FACs, Upward or Downward, in $\mu\text{A}/\text{m}^2$) through Equation 1 denoting the three regions of interest - low and high FAC bins used to estimate the values of A_0 and A_1 , while the region in between these bins defining the curve using regression of A_2 . (b) An example log-log plot of the AMIE data showing the scatter of Hall Conductance versus Upward Field Aligned Currents, at magnetic latitude of 68° and magnetic local time (MLT) 23 in the nightside auroral zone. Alongside the data spread, the regression line is plotted in red with the dot-dashed lines exhibiting the low and high FAC bins. (c) The distribution of AMIE data from 2003 showing the scatter of Hall Conductance versus all Field Aligned Currents plotted along the line plots of RLM and CMEE, denoted in blue and red respectively, at 68° magnetic latitude and 23 MLT. Note this distribution plot is in linear scale compared to the similar plot part (b), which is in logarithmic scale.

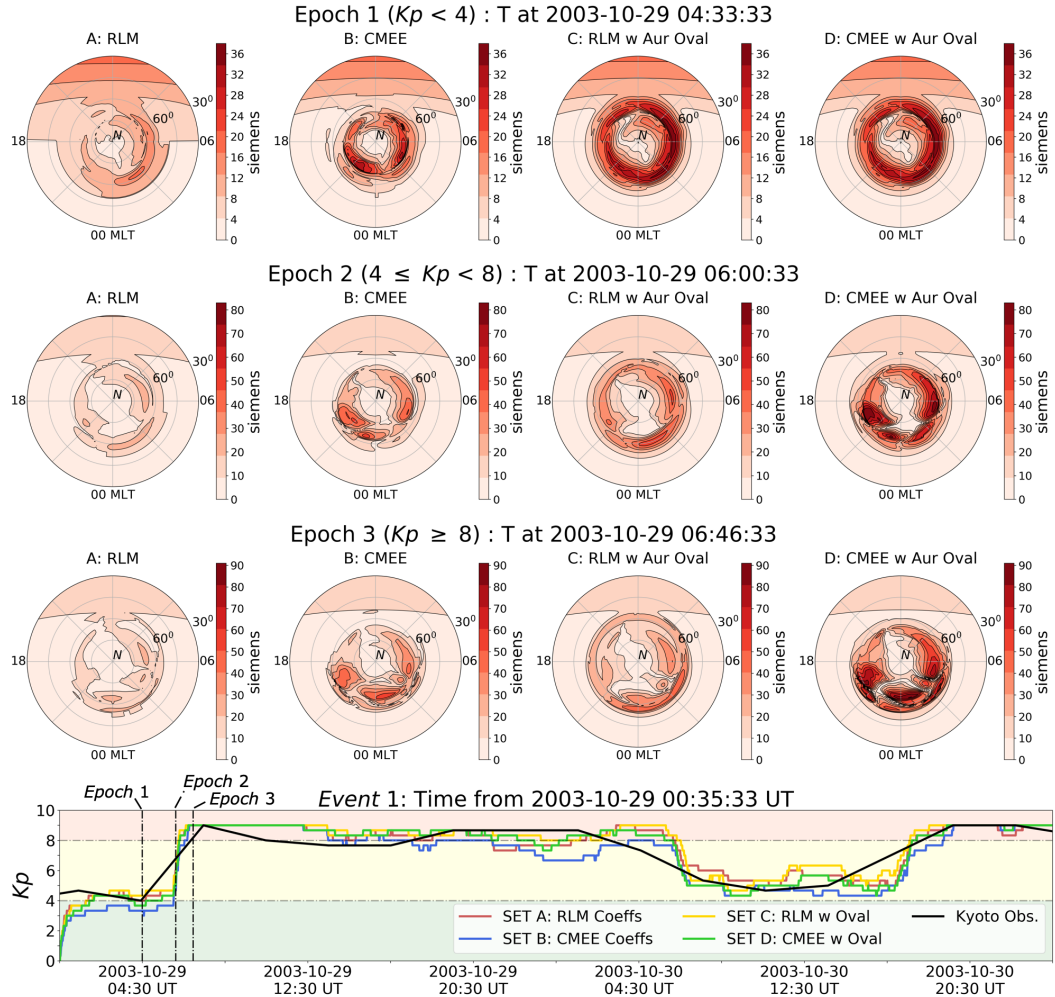


Figure 4. A comparison of Hall conductance values from different conductance model variants. Dial plots from (left to right) simulation sets A, B, C and D at time instances during Event 1 (Epoch 1, Top Row) when $K_p < 4$, (Epoch 2, Second Row) when $4 \leq K_p < 8$, and (Epoch 3, Third Row) when $K_p \geq 8$. (Bottom Subplot) Comparison of K_p from the Kyoto Observatory (in black) against simulated K_p from simulation sets A (in red), B (in blue), C (in gold) and D (in green). Additionally, the plot background is coloured by the K_p , green signifying $K_p < 4$, yellow signifying $4 \leq K_p < 8$, and red signifying $K_p \geq 8$.

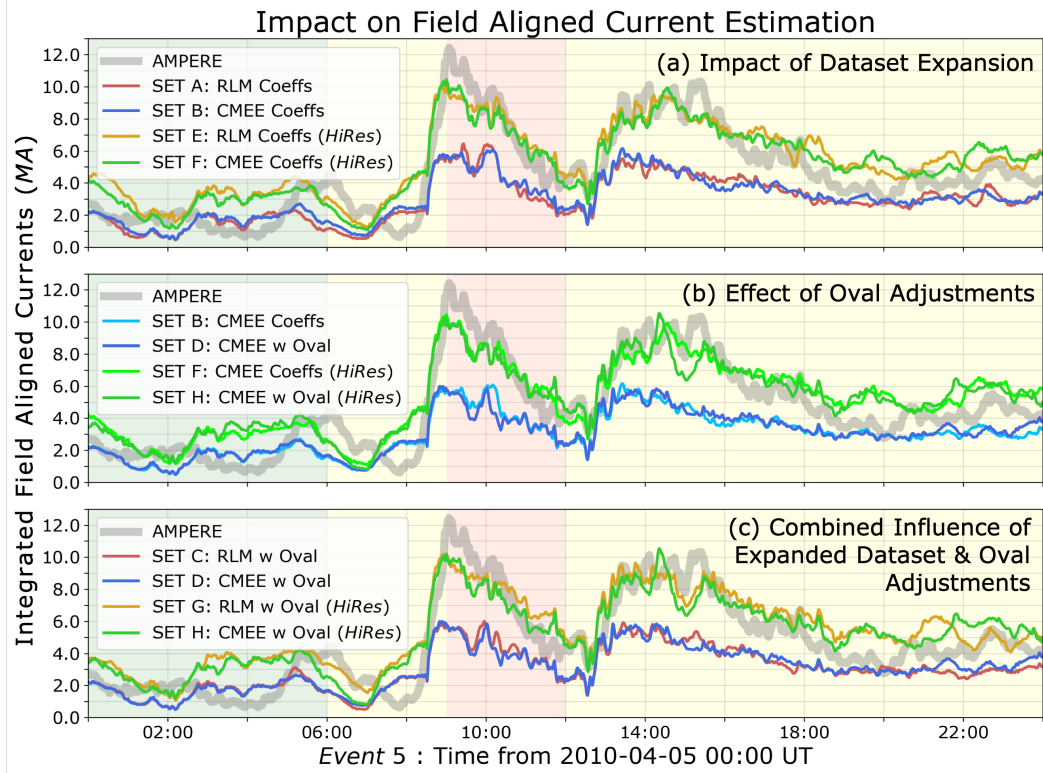


Figure 5. Time series comparison of integrated field aligned currents (iFACs) for Events 5 spanning the storm main phase from AMPERE (gray line) and the eight simulation sets of the SWMF. Goal of each frame: Top Frame (a) illustrates the impact of dataset expansion on iFACs by comparing Sets A (in red), B (in blue), E (in gold) and D (in green). Middle Frame (b) displays the effect of oval adjustments by comparing Sets B (in light blue), D (in blue), F (in light green) and H (in green). Bottom Frame (c) presents the combined influence of dataset expansion and oval adjustments by comparing Sets C (in red), D (in blue), G (in gold) and H (in green). The plot background is coloured by the K_p , green signifying $K_p < 4$, yellow signifying $4 \leq K_p < 8$, and red signifying $K_p \geq 8$.

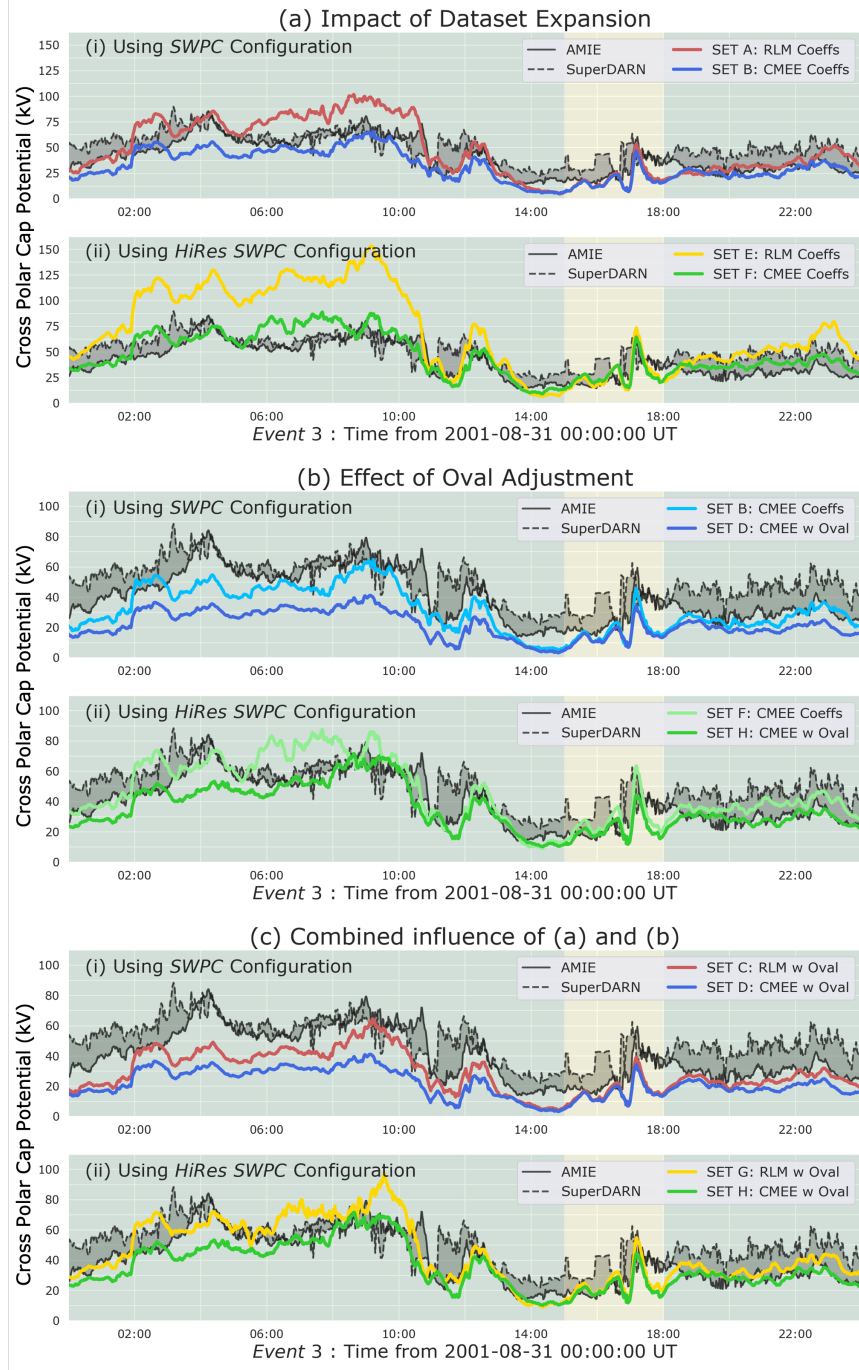


Figure 6. Time series comparison of cross polar cap potential (CPCP) for Event 3 comparing observations from AMIE, SuperDARN, and the eight configurations of the SWMF. Traces show AMIE in solid black, SuperDARN in dashed black, with the difference region between the datasets coloured gray. The SWMF simulations are coloured similarly to Figure 5. Goal of each frame: Top Frame (a) illustrates the impact of dataset expansion on iFACs by comparing (i) Sets A & B in upper panel, and (ii) Sets E & D in bottom panel. Middle Frame (b) displays the effect of oval adjustments by comparing (i) Sets B & D in upper panel, and (ii) F & H (in green) in bottom panel. Bottom Frame (c) presents the combined influence of dataset expansion and oval adjustments by comparing (i) Sets C & D in top panel, and (ii) G & H in bottom panel. The plot background is coloured by the K_p , green signifying $K_p < 4$, and yellow signifying $4 \leq K_p < 8$.

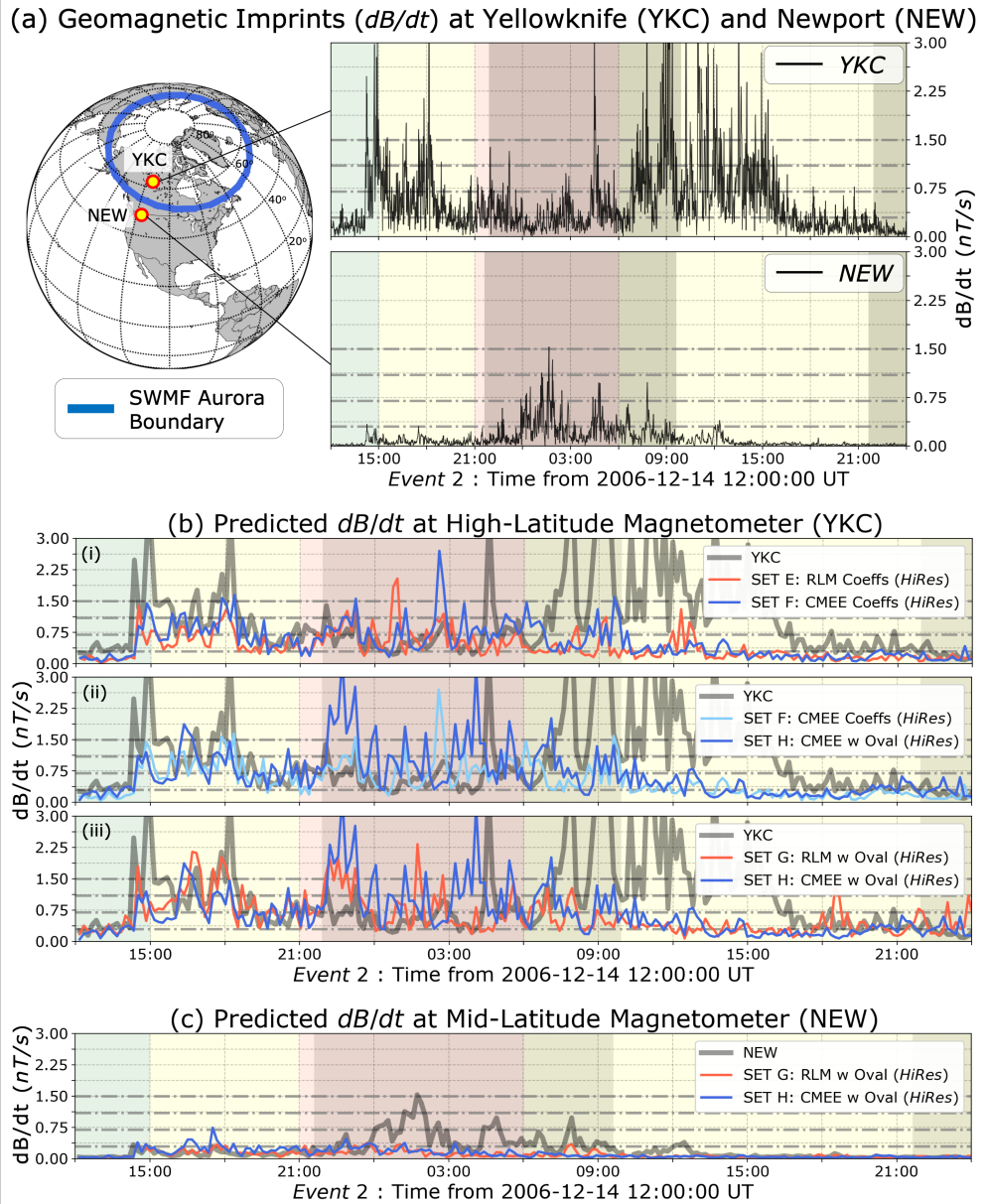


Figure 7. Impact of changes to the auroral conductance on dB/dt predictions - (a) (Left) Location of Yellowknife (YKC) and Newport (NEW) magnetometer stations mapped in geographic coordinates with the SWMF auroral boundary demarcated using the thick blue line. (Right) Raw dB/dt observations at a 1-minute cadence at YKC and NEW. (b) Comparison of max-filtered predicted dB/dt from *Hi-Res* SWMF simulations against similarly filtered dB/dt observations at Yellowknife (YKC). Goal of each panel: Top panel (i) shows impact of coefficients by comparing simulation sets E (in red) and F (in blue). Middle panel (ii) illustrates the impact of oval adjustments by comparing sets F (in light blue) and H (in blue). Bottom panel (iii) compares sets G (in red) and H (in blue). Observations are shown as a thick, grey curve. (c) Comparison of max-filtered predicted dB/dt from sets G (in red) and H (in blue) against observations (thick, grey curve). The dot-dashed lines in the line plots are markers of the thresholds used in the *Pulkkinen2013* study for their event-based analysis. The background of the line plots are coloured by K_p , similarly to Figure 5. The dark shaded background regions are times when the respective magnetometer was in the nightside.

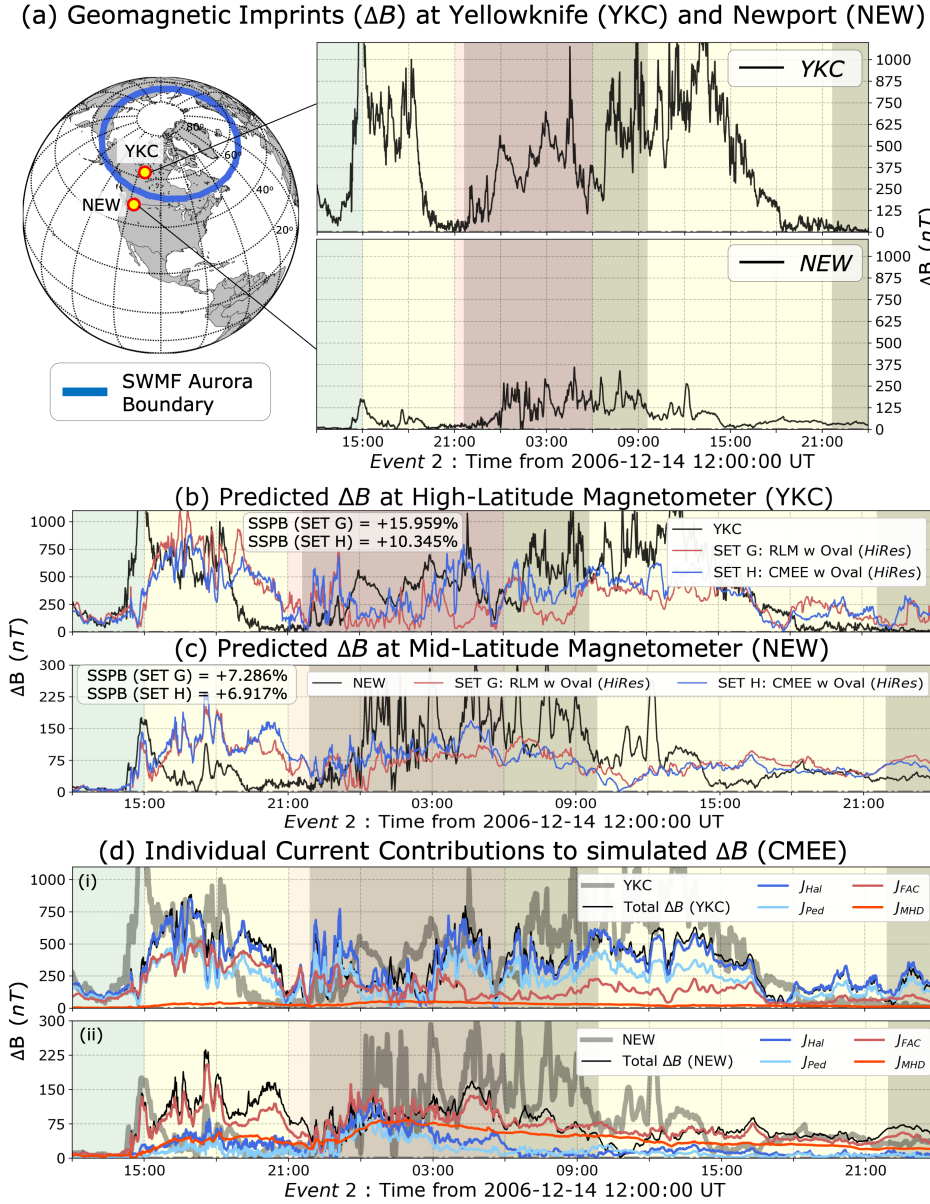


Figure 8. Impact of changes to the auroral conductance on ΔB predictions - (a) (Left) Location of Yellowknife (YKC) and Newport (NEW) magnetometer stations mapped in geographic coordinates with the SWMF auroral boundary demarcated using the thick blue line. (Right) Raw ΔB observations at a 1-minute cadence at YKC and NEW. (b) Comparison of predicted ΔB from *Hi-Res* SWMF simulations against observations at YKC, and (c) at NEW. Both subplots compare results from simulation sets G (in red) and H (in blue) against observations (in black). (d) Comparing contribution of individual current sources in the simulated ΔB at (i) YKC and (ii) NEW. The contributions from Hall currents are in blue, Pedersen currents in light blue, FACs in red, and MHD in orange. The background of the line plots are coloured by K_p , similarly to Figure 5. The dark shaded background regions are times when the respective magnetometer was in the nightside.

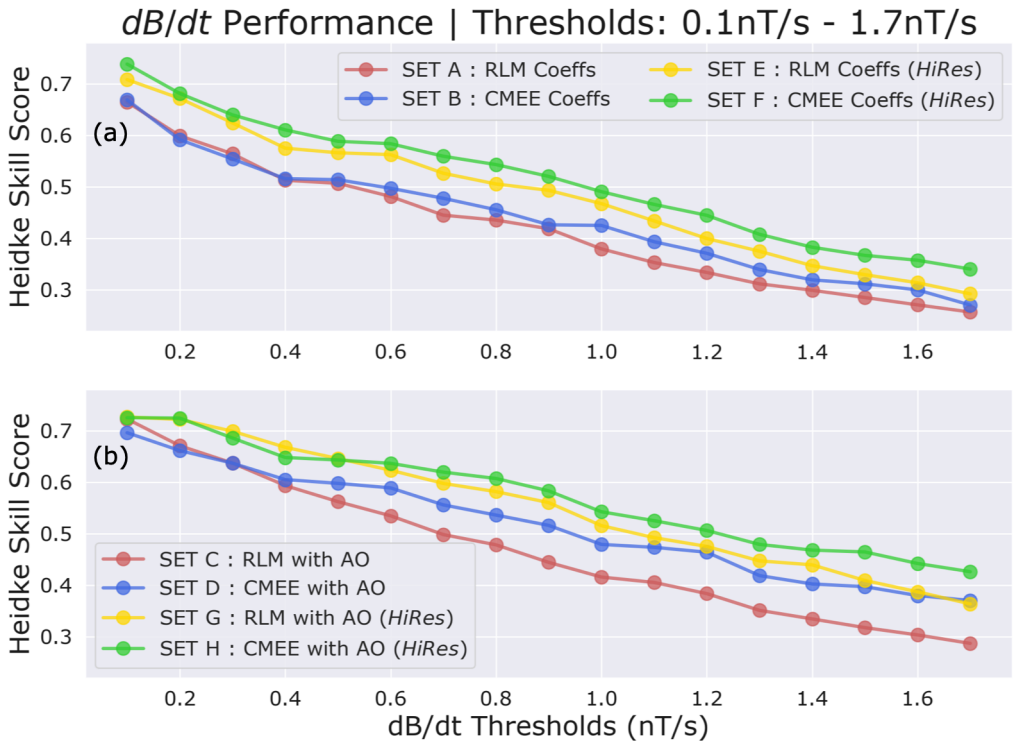


Figure 9. Heidke Skill Score (HSS) Performance of all SWMF simulation variants at ascending dB/dt predictions for all events from Table 1(a). (a) Comparison of simulation sets A (in red), B (in blue), E (in yellow) and F (in green) illustrating the impact of dataset expansion. (b) Comparison of simulation sets C (in red), D (in blue), G (in yellow) and H (in green) displaying the overall impact of dataset expansion with oval adjustments. Note the y-axis in (a) and (c) does not start at zero.

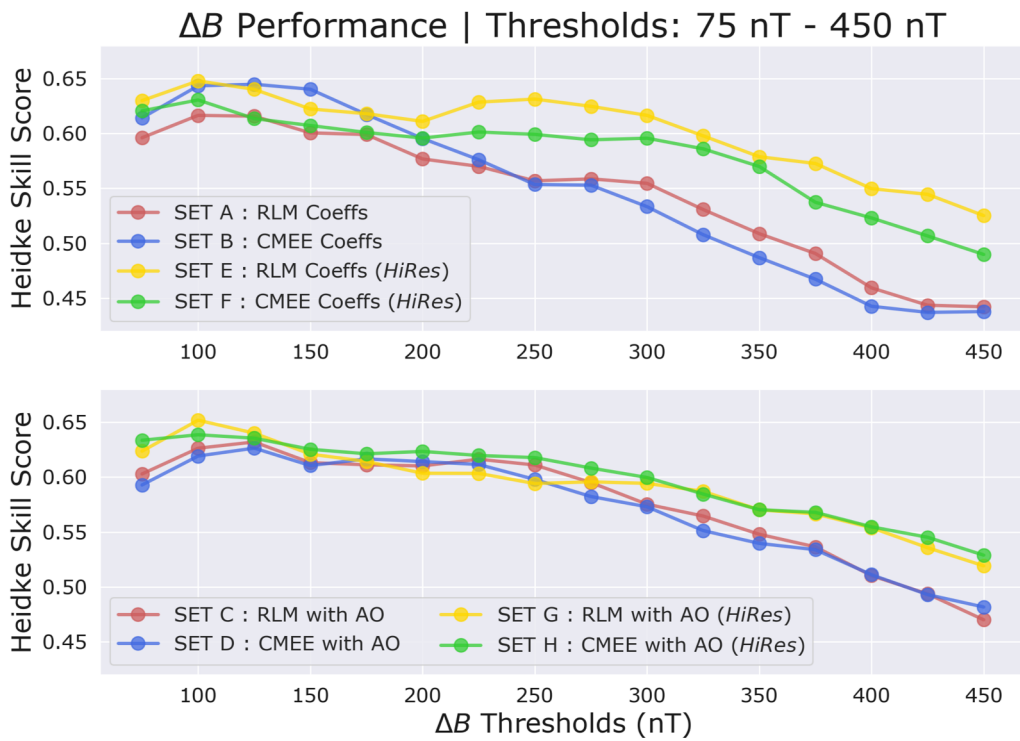


Figure 10. HSS Performance metrics of all SWMF simulation variants at ascending ΔB predictions for all events from Table 1(a). The format is similar to Figure 9. Note the y-axis in (a) and (c) does not start at zero, and spans a smaller range than Figures 9(a) and (c).